UNIVERSIDADE FEDERAL DE MINAS GERAIS
Instituto de Ciências Exatas
Programa de Pós-graduação em Física

Aroldo Ribeiro Lopes Neto

Enhancement Factor on Tip-Enhanced Raman Spectroscopy

Belo Horizonte
2020

Aroldo Ribeiro Lopes Neto

Enhancement Factor on Tip-Enhanced Raman Spectroscopy

Dissertação apresentada ao Programa de Pós-Graduação em Física do Instituto de Ciências Exatas da Universidade Federal de Minas Gerais como requisito parcial para obtenção do título de Mestre em Ciências.

Orientador: Prof. Ado Jorio de Vasconcelos
Coorientador: Prof. Luiz Gustavo de Oliveira Lopes Cançado

Belo Horizonte
2020

Dados Internacionais de Catalogação na Publicação (CIP)

L864e Lopes Neto, Aroldo Ribeiro.
Enhancement factor on tip-enhanced Raman spectroscopy / Aroldo Ribeiro Lopes Neto. – 2020.
55f., enc. : il.

Orientador: Ado Jorio de Vasconcelos.
Coorientador: Luiz Gustavo de Oliveira Lopes Cançado.
Dissertação (mestrado) – Universidade Federal de Minas Gerais, Departamento de Física.
Bibliografia: f. 39-46.

1. Espectroscopia de Raman, teses. 2. Grafeno. 3. Scanning probe microscopy.
I. Título. II. Vasconcelos, Ado Jorio de. III. Universidade Federal de Minas Gerais, Departamento de Física.

CDU – 543.424.2 (043)

Ficha catalográfica elaborada por Romário Martins – CRB6 3595
Biblioteca Professor Manoel Lopes de Siqueira – Departamento de Física - UFMG

UNIVERSIDADE FEDERAL DE MINAS GERAIS

A presente dissertação, intitulada **“Enhancement Factor on Tip-Enhanced Raman Spectroscopy”** de autoria de **AROLDO RIBEIRO LOPES NETO**, submetida à Comissão Examinadora, abaixo-assinada, foi aprovada para obtenção do grau de **MESTRE EM FÍSICA** em 29 de maio de 2020.

Belo Horizonte, 29 de maio de 2020.

Prof. Ado Jório de Vasconcelos
Orientador do estudante
Departamento de Física/UFMG

Prof. Luiz Gustavo de Oliveira Lopes Cançado
Coorientador do estudante
Departamento de Física/UFMG

Prof. Leonardo Teixeira Neves
Departamento de Física/UFMG

Prof. Wagner Nunes Rodrigues
Departamento de Física/UFMG

Documento assinado eletronicamente por **Ado Jorio de Vasconcelos**, **Presidente de comissão**, em 29/05/2020, às 16:49, conforme horário oficial de Brasília, com fundamento no art. 6°, § 1°, do Decreto n° 8.539, de 8 de outubro de 2015.

Documento assinado eletronicamente por **Leonardo Teixeira Neves**, **Professor do Magistério Superior**, em 29/05/2020, às 22:52, conforme horário oficial de Brasília, com fundamento no art. 6°, § 1°, do Decreto n° 8.539, de 8 de outubro de 2015.

Documento assinado eletronicamente por **Luiz Gustavo de Oliveira Lopes Cancado**, **Professor do Magistério Superior**, em 30/05/2020, às 12:28, conforme horário oficial de Brasília, com fundamento no art. 6°, § 1°, do Decreto n° 8.539, de 8 de outubro de 2015.

Documento assinado eletronicamente por **Wagner Nunes Rodrigues**, **Diretor(a)**, em 01/06/2020, às 14:22, conforme horário oficial de Brasília, com fundamento no art. 6°, § 1°, do Decreto n° 8.539, de 8 de outubro de 2015.

Agradecimentos

Dedico essa dissertação as minhas três mães: vovó Marlene, mamãe Catarina e titia Cristina. O que seria de mim sem elas?

Inicio os agradecimentos pedindo desculpas a todas as pessoas que fizeram parte da minha vida e que não mencionei aqui. Isto é definitivamente uma injustiça e espero que me perdoem.

A primeira pessoa a qual quero prestar agradecimentos é meu orientador, o Prof. Ado Jório. Um amigo que me espelho tanto profissionalmente quanto pessoalmente. Um exemplo de dedicação e que sempre espera o melhor das pessoas. Lembro-me de vários conselhos seus antes de decisões importantes da minha vida, sempre muito calmo e humano, ponderando minha perspectiva, minhas ambições e limitações. Levo comigo uma frase dele que é sempre útil em momentos incertos da vida: cala a boca e rema.

Agradeço também ao Prof Luiz Gustavo, meu co-orientador. Essa dissertação não seria concebida sem nossas inúmeras discussões sobre óptica, e em especial sobre seu famoso PRX. Impossível não mencionar também as festas em sua casa, onde Mutantes e Rolling Stones fazia parte do som ambiente.

Lembro aqui do Cassiano que definitivamente mudou minha vida me ensinando a programar. Meu amigo arquiteto, que programa, que já foi designer, e que hoje é Doutor em Engenharia e pesquisador - além de pai de dois filhos. Lembro também do Prof. Xubaca e aos meus amigos de LabNS que marcaram minha vida.

Tenho gratidão por todos os meus amigos que estiveram comigo sempre. Em especial a Laíse, Luiz e a Laiz. Os dois primeiros são pessoas extremamente importantes na minha vida que me fizeram ser quem eu sou hoje. E a Laiz minha esposa e melhor companhia. Ela me apoiou em exatamente cada segundo do meu mestrado e de tantos outros momentos da minha vida.

Também tenho gratidão aos meus amigos e amigas da Amônia. Eles e elas sabem o sinto por todas. Neste contexto de término de dissertação, queria mencionar a ajuda do Thales e do André que foram fundamentais para eu conseguir concluí-la.

Por fim, agradeço a Melzinha que não cansa de demonstrar amor por mim.

Resumo

A espectroscopia Raman com aumento por ponta (do inglês *tip-enhanced Raman spectroscopy* - TERS) é uma técnica que combina o potencial da espectroscopia Raman de fornecer informações químicas sobre uma amostra com a capacidade da microscopia de varredura por sonda (do inglês *scanning probe microscopy* - SPM) de detalhar aspectos espaciais com resolução da ordem de nanômetros. A nanoantena é o dispositivo por trás do aumento do TERS, sendo geralmente feitas por um metal com propriedades plasmônicas e tendo o ápice com dimensões nanométricas. Existem várias técnicas diferentes para produzi-las, e algumas proporcionam aumentos maiores que outras. Porém, vários outros fatores não relacionados com a ponta também contribuem para esse aumento, e não há consenso sobre uma definição do fator de aumento intrínseco (f_e) fornecido pela nanoantena, que isolaria esses outros fatores. A complexidade reside na ausência de uma definição teórica adequada para esse fator e de um experimento capaz de medir resultados consistentes para medi-la. Esta dissertação propõe um protocolo capaz de medir este fator de aumento intrínseco. A necessidade dessa definição vem da rápida evolução tecnológica na construção dessas antenas, e da dificuldade de comparar nanoantenas fabricadas por cada uma dessas diferentes formas. Primeiramente, nesta dissertação foram descritos os aspectos teóricos da curva de aproximação, usados para ajustar os dados experimentais para se determinar f_e. Posteriormente, foi proposta um protocolo capaz de medir o fator de aumento intrínseco f_e que deverá ser realizado com uma amostra com um espalhamento Raman de campo próximo bem descrito na literatura, integrado em um dispositivo com outras especificações que permitem caracterizar e otimizar o sistema de medição. Por fim, no capítulo de conclusão, duas possíveis aplicações para o protocolo são descritas.

Palavras-chave: nanoantena; fator de aumento; grafeno; material de referência; tip-enhanced Raman spectroscopy.

Abstract

Tip-enhancend Raman spectroscopy (TERS) is a technique that combines the Raman spectroscopy capability of providing chemical information with a Scanning Probe Microscopy (SPM) potential to resolve spatially details in the order of nanometers. The specific device behind the TERS is the nanoantenna. The nanoantennas are usually made of metal, and their tip apex is of the order of only a few nanometers. Also, there are several different ways to produce nanoantennas that yield enhancement in the scattered field. However, there is up to date no agreement on what is the intrinsic enhancement factor (f_e) provided by the nanoantenna. The complexity resides both on the lack of a proper theoretical definition and of a reliable experimental procedure for measuring it. This dissertation is dedicated to propose a protocol to measure the f_e. The necessity comes from the rapid development of TERS and the necessity to establish the tailable factors that affect the enhancement properties of these tips. First, the theoretical description of the tip-sample interaction is investigated, as well as how it behaves by varying the sample and tip parameters. Later, a tool for measuring the intrinsic f_e and a protocol is discussed, which should be performed in a reference material made of a well-defined near-field Raman scattering material, integrated with other specificities that allows measuring all the parameters necessary to fully optimize and characterize the measuring system. In the conclusion chapter, two applications of the protocol are described.

Keywords: nanoantenna; enhancement factor; graphene; reference material; tip-enhanced Raman spectroscopy.

Contents

Chapter 1

Introduction

When a nanoantenna is positioned on the light scattering region of a sample, it might amplify the signal. The Tip-enhanced Raman Spectroscopy (TERS) is one of the techniques that make use of this phenomenon to intensify the usually low Raman signal by having a Scanning Probe Microscopy (SPM) system positioning this nanoantenna in the desired location. Thus, the scattered light on the area below the nanoantenna apex is enhanced providing both chemical and topographic information with a nanometric spatial resolution.

This dissertation is dedicated to understand the underlying phenomena of the Raman signal enhancement by the nanoantenna and to propose technological developments related to this knowledge. This Introduction chapter has a brief description of TERS in graphene, which is the prototype material utilized for measuring tip enhancement. It is followed by an explanation of the nanoantennas' role in the enhancement and a presentation of their fabrication methods. The following chapter, namely Review of the Enhancement Factor Measurements, is dedicated to review the problem of defining the enhancement factor of a nanoantenna, and to argue why they are problematic. The third chapter, entitled Theoretical Description of a Tip-approach Curve describes the theory to calculate the signal intensity in a TERS experiment, and the results are used to define the intrinsic enhancement factor f_e and to derive The Calibration Device and Measurement Protocol for measuring f_e. The Conclusion highlights two examples of protocol applications: measuring enhancement factor of a tip and accessing other 2D material properties, i.e. as the phonon spatial coherence length L_c.

1.1 Conventional Raman Spectroscopy versus TERS

TERS is able to provide chemical information with an improved spatial resolution when compared to conventional Raman spectroscopy [1–4]. In order to illustrate this, Fig.1.1 shows in (a) a conventional Raman image and (b) the TERS-image of the same carbon nanotube (CNT) serpentine, as measured in Ref. [5]. The conventional Raman hyperspectra resulted in a blurred image with a spatial resolution of $400\ \mu m$, the size of the laser spot. Then, the TERS

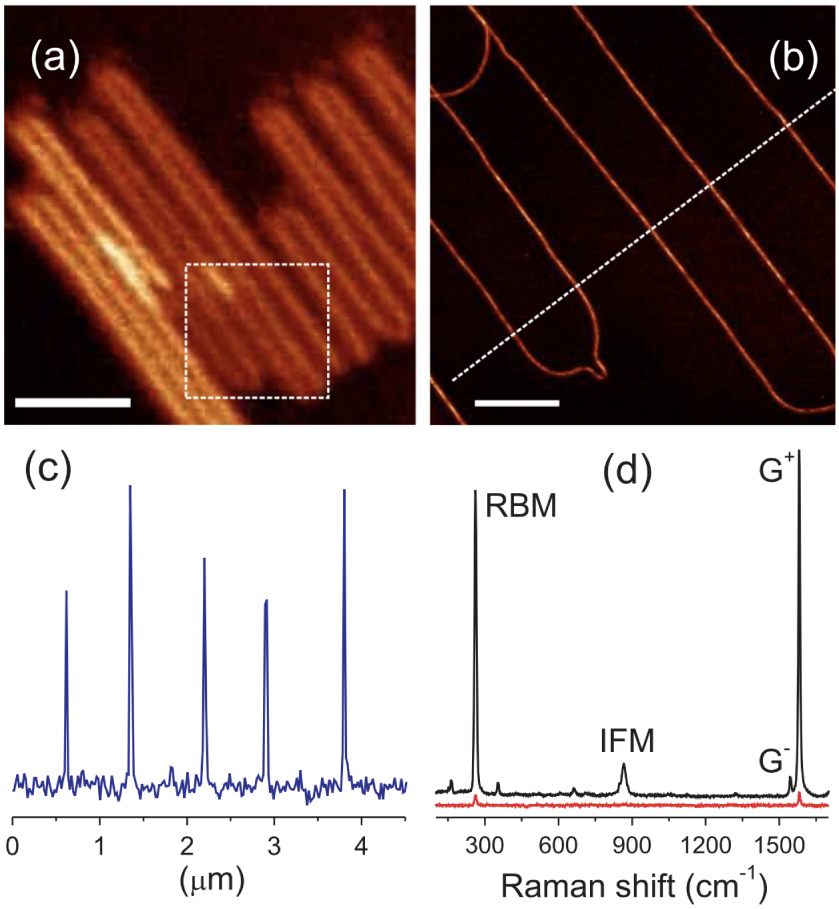

Figure 1.1: Conventional Raman spectroscopy image versus TERS image
(a) Conventional confocal Raman of a carbon nanotube serpentine. (b) TERS image of the boxed region in (a). Reproduced from Ref. [5]

was performed in the box region of 1.1(a): the result shown in 1.1(b) evidences a more defined CNT structure, revealing details that were not observable in the conventional Raman image. The spatial resolution was improved to 25 *nm*, which is roughly the size of the nanoantenna apex [5].

Given that TERS is a non-destructive and label-free procedure to access both chemical and topographic information with a high spatial resolution, several applications have been reported: single-cell membranes components dynamics were measured [6–8]; single RNA-bases were labeled [9–11]; single virus particles were detected [12–14]; protein structural differences were observed [15–17]; strain on silicon devices and carbon-based devices were characterized [18–20].

1.2 The Nanoantenna

The key technological device behind the TERS effect is the nanoantenna. When this sharp metal tip is added to the SPM system and illuminated by a light source, it occurs the

coupling of the photons with the free oscillation of the electrons on the metal surface, forming the surface plasmon-polariton (SPP) [21]. Due to the shape of the nanoantenna, the SPP drives the photons to the vicinity of the nanoantenna's tip, creating a photon reservoir in a region defined by the tip radius r_{tip} [22, 23]. Consequently, it generates a strong enhancement on the electric field $|\mathbf{E}|$ confined to a region proportional to the area below the nanoantenna's tip apex [22–24]. Also, due to the sharpness of the tip apex, the lightning rod effect also plays a non-neglected role in the enhancement [25].

The polarization of the laser beam that excites the nanoantenna also plays a role in the enhancement. The enhancement is 10^3 larger when the electric field has a strong component along the nanoantenna axes, configuration obtained when the radially polarized laser beamis focused using a high numerical aperture (N.A.) lens [23, 26, 27].

Another important aspect of TERS comes from the fact that the nanoantenna is positioned only a few nanometers above the sample, working in the near-field regime. In this regime, the evanescent electric field emitted by the nanoantenna is now able to excite the sample [23]. The other way around is also true, the nanoantenna is able to collect the near-field Raman scattered light from the sample and to transform the information contained in a propagating far-field via the oscillations of the SPP. Therefore, the technique is able to capture the interference of the light scattered by the phonons because the photons have a correlation length L_c in the order of tens of nanometers, accessible by the nanoantenna in the near-field regime [28–31].

1.2.1 Nanoantenna Fabrication

The efficiency of the TERS relies on having a nanoantenna with a powerful enhancement factor (EF), therefore, it is desirable from a fabrication standpoint to develop methods to produce tips with highest EF, and also in a cheap and reproducible fashion.

One fairly commonly used technique to produce these tips is the lamella-dropoff electrochemical etching method [32–35]. This method consists of dividing 100 μm thick gold or silver wire in an etching solution and passing a DC current through the wire. The applied tension is then turned off when a drop in the current is detected, meaning that the immersed part of the wire has etched enough to form a tip. Images a) and b) of Fig.1.2 show the Scanning Electron Microscopy (SEM) image of one nanoantenna produced by this etching procedure.

Other techniques have been developed to increase the nanoantenna EF of by exploring cavity-induced resonance conditions of the SPP, via localized surface plasmons resonance (LSPR). One of these consists in producing a groove near the apex of a gold etched tip by using a focused ion beam (FIB) setup [36]. In the bottom of Fig.1.2 there is a comparison of the Raman intensity enhancement provided by the same tip before the milling, on the left (c), and after the milling, on the right (d). By comparing the height of the blue lines before and after the milling, it is confirmed the positive effect of the LSPR on the enhancement of the signal.

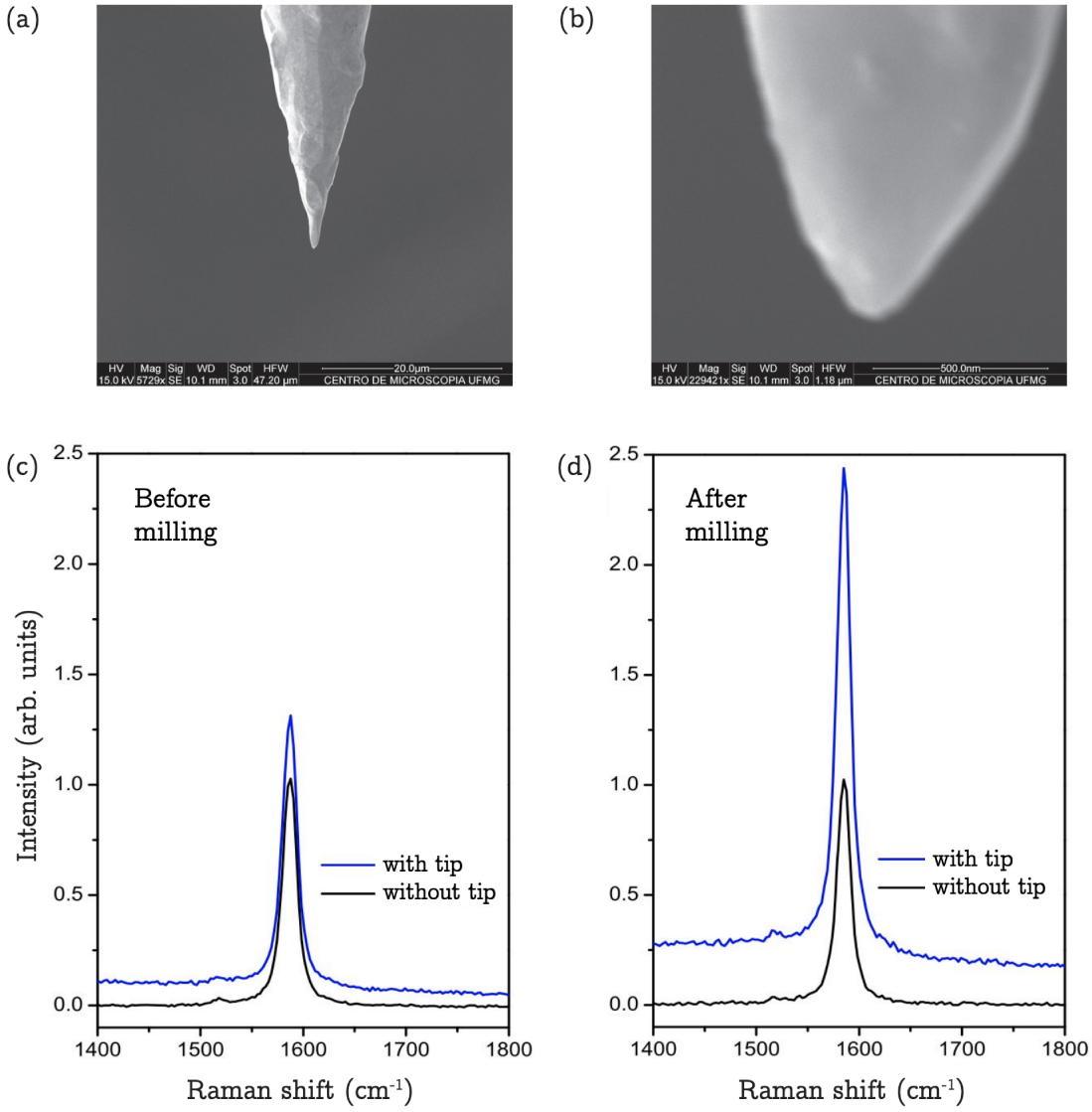

Figure 1.2: Top: SEM imagea of an electrochemically etched tip. Bottom: Raman intensity enhancements before and after the FIB milling
a) and b) figures show SEM images of a nanoantenna fabricated by the lamella-dropoff electrochemical etching method using HC*l* as the enchant. The b) figure is a zoom of the tip apex, estimated to be on the order of 30*nm* in diameter. The two bottom images were taken from Ref [36], where c) shows the enhancement of one tip made by a similar electrochemical process. And the d) shows a greater TERS enhancement by the same tip after FIB milling.

Many other techniques address the challenge to produce these nanoantennas. Some of them involve coating a metal tip by chemical deposition of gold or silver in a standard AFM tip [37–39], or fabricating nano-pyramids by taking advantage of the anisotropic etching of crystalline silicon and then depositing gold on the pyramid-shaped structure [40, 41]. It is also possible to tune the enhancement by creating FIB-induced LSPR conditions [42].

With all these possible methods to create nanoantennas, the question to answer is which was has the greatest EF. The problem is that many variables that are not related to the nanoantenna can change the field enhancement. For instance, incident laser wavelength, specific metal, polarization and incident angle, alignment, etc, they are all instrumental factores that might influence in the enhancement [43–45]. Additionally, it is known that the substrate material and roughness influences the intensity [46, 47]. Furthermore, different authors calculate the EF in a different way, under different experimental condition and, consequently, it is not possible to infer which nanoantenna provides the greatest enhancement.

The main goal of this dissertation is to demonstrate a standardized way to measure the intrinsic enhancement factor of the nanoantenna, f_e [48]. This protocol makes it possible to compare two different nanoantennas by defining an intrinsic enhancement field factor f_e. In the next chapter, the literature will be revised on the current definitions on how to measure the EF.

Chapter 2

Review of the Enhancement Factor Measurements

As stated in the end of the introductory chapter, several aspects of the configuration of a TERS experiment might change the observed enhancement. It is indeed a challenge to isolate the effect provided by the nanoantenna itself. In this chapter, it is presented a review on the most broadly used definition of $EnhancementFactor$, and the related problems are discussed.

2.1 The Enhancement Factor in the Literature

The simplest way to evaluate the nanoantenna in terms of its field enhancement EF is to measure the *contrast*, which is defined as the ratio of signal intensity measured with the nanoantenna and without it [40]:

$$\begin{aligned} contrast &= \frac{I_{near\ field}}{I_{far\ field}} \\ &= \frac{I_{with\,tip} - I_{without\,tip}}{I_{without\,tip}} \\ &= \frac{I_{with\,tip}}{I_{without\,tip}} - 1 \end{aligned} \tag{2.1}$$

where $I_{near\ field}$ is defined as the Raman peak intensity due only to the interaction of the nanoantenna with the scattering material, which is the signal measured while the tip is interacting with the sample, $I_{with\,tip}$, subtracted by the signal when the tip is not interacting with the sample ($I_{without\,tip}$). On the other hand, $I_{far\ field}$ is the intensity measured without the nanoantenna enhancement, which equals the intensity measured without the tip, $I_{without\,tip}$.

While the contrast is sufficient to determine the EF in the case of an ideal zero-dimensional scatterer, such as a single molecule, in the case of a sample dispersed in a surface

or volume, the amount of material contributing to the far-field and near-field signals have to be evaluated. The EF then is defined as the product of the contrast and the effective illumination area ratio between near- and far-field, namely the geometric factor GF, with

$$EF = contrast \times GF. \tag{2.2}$$

The GF evaluation depends on sample geometry, illumination pattern and tip properties. Considering a sample homogeneously distributed on a two-dimensional surface, we name $A_{focus} = \pi r_{focus}^2$ as the illumination area of the focused laser beam and $A_{tip} = \pi r_{tip}^2$ as the illumination area of the tip apex on the scattering surface. GF can then be evaluated as

$$GF = \frac{A_{focus}}{A_{tip}} = \frac{r_{focus}^2}{r_{tip}^2}. \tag{2.3}$$

Although largely accepted due to its simplicity [22,49–53], this "back-to-the-envelop" theory is problematic. Different samples in different setups, and even different scattering systems result in different contrast values for the same nanoantenna. Table 2.1 exemplifies how changes on r_{tip} and r_{focus} drastically vary the EF evaluation. Considering, without loss of generality, a measurement resulting in a $contrast$ of 2.1, using a tip of radius $(15 \pm 5)nm$ and laser focus radius of $(200 \pm 40)nm$, the resulting EF using equation 2.2 varies from *94* to *588*.

In Ref. [47] the authors reviewed several articles, each of them with a different TERS experiment configuration. All of them resulted in different $contrast$ and EF values. The results are reproduced with adaptations in Fig.2.1. It is emphasized in the figure the different SPM based systems used in each work, where the dark green and dark red represents respectively the EF and the $contrast$ of a TERS experiment having the SPM based on atomic force microscopy (AFM), and light green and light red represents the same properties but for SPM system based on scanning tunneling microscope (STM) [54].

Table 2.1: EF values as a function of laser spot radius r_{focus} and tip radius r_{tip} calculated using Eqs. 2.2 and 2.3 for a $contrast$ = 2.10.

		Laser spot radius (nm)				
		160	**180**	**200**	**220**	**240**
Tip Radius (nm)	**15.0**	261	331	408	494	588
	17.5	192	243	300	363	432
	20.0	147	186	230	278	331
	22.5	116	147	181	219	261
	25	94	119	147	178	211

When comparing different nanoantennas among the references in Fig.2.1, it is not possible to conclude exactly which one has the greatest intrinsic enhancement factor. For instance, in (m Mehtani 2005) Ref. [55] it is reported a lower $contrast$ than in (o Neugebauer 2006) Ref. [56], but the EF values are in the same order of magnitude.

Consequently, different authors may define the enhancement factor slightly differently, depending on the application [51–53]. Also, there isn't an agreement in the TERS research community whether the EF is related to the experimental setup [22, 47, 49] or to the tip itself [50]. In order to have TERS as an useful nanomaterials' characterization technique, it is urgent to minimize the arbitrariness in the definition of enhancement factor of a nanoantenna, providing a protocol to compare different nanoantennas in terms of their enhancement factor.

The next chapters will be dedicated to derive the protocol to measure the intrinsic nanoantenna enhancement f_e. This protocol is based on measuring the TERS intensity as a function of the tip-sample distance Δz (named tip-approach procedure) of a graphene-based reference material. Subsequently, the experimental data is adjusted by the tip-approach curve $I_{\Gamma}^{TERS}(\Delta z)$, which represents the Raman scattering of intensity I of the phonons of symmetry Γ, given a tip-sample separation of Δz. In the following section, the theory behind the tip-approach curve will be presented.

Figure 2.1: Several TERS experiment and their calculated Contrast and Enhancement Factor, adapted from Ref. [47]
a Stöckle 2000 [1]; b Anderson 2000 [2]; c Hayazawa 2000 [3]; d Pettinger 2000 [57], e Hayazawa 2002 [58]; f Hayazawa 2002b [59]; g Pettinger 2002 [60]; h Hayazawa 2003 [61]; i Bulgarevich 2004 [52]; j Pettinger 2004 [4]; k Ren 2004 [35]; l Pettinger 2005 [62]; m Mehtani 2005 [55]; n Vannier 2006 [63]; o Neugebauer 2006 [56]; p Domke 2006 [64]; q Yeo 2007 [38]; r Zhang 2010 [65]; s Steidtner 2007 [66]; t Steidtner 2008 [67]; u Stadler 2010 [34]; v Chaigneau 2011 [68].

Chapter 3

Theoretical Description of a Tip-approach Curve

In this chapter, the function $I_{\Gamma}^{TERS}(\Delta z)$, i.e. the tip-approach curve will be derived, following the steps published in Ref. [29]. The objective is not going through all the numerical calculations, but rather expose the necessary assumptions and physics related phenomena.

3.1 TERS system model

In order to derive $I_{\Gamma}^{TERS}(\Delta z)$, the TERS system is modeled by three components: the nanoantenna, a graphene and a detector. The first one is located at $\mathbf{r}' = (0, 0, z)$, the graphene is assumed to occupy all the xy-plane at $(x, y, 0)$ and the detector is located infinitely distant from this plane, as illustrated in Fig.3.1. This system is illuminated by an incident electric field $\mathbf{E}_0$ of frequency ω. This electric field is assumed to have the component along the nanoantenna's tip E_z greater than the components on the xy-plane, to mimic a radial polarized laser passing through a highly focusing objective lens [23, 26, 27].

The next step is to calculate how these components interacts with each other via the scattering process.

3.1.1 Scattered Electric field

The resulting scattered electric field $\mathbf{E}^s$ can be calculated by considering a surface $\mathbb{D}$ (it could also be generalized by a volume) composed by infinitesimally small induced dipoles $\mathbf{p}(\mathbf{r}, \omega)$ and summing all their contribution to the scattered field and a Green's function $\overleftrightarrow{G}$ that represents the evolution of the radiation field from a point $\mathbf{r} \in \mathbb{D}$ to another unspecified point $\mathbf{q} \notin \mathbb{D}$ [69]

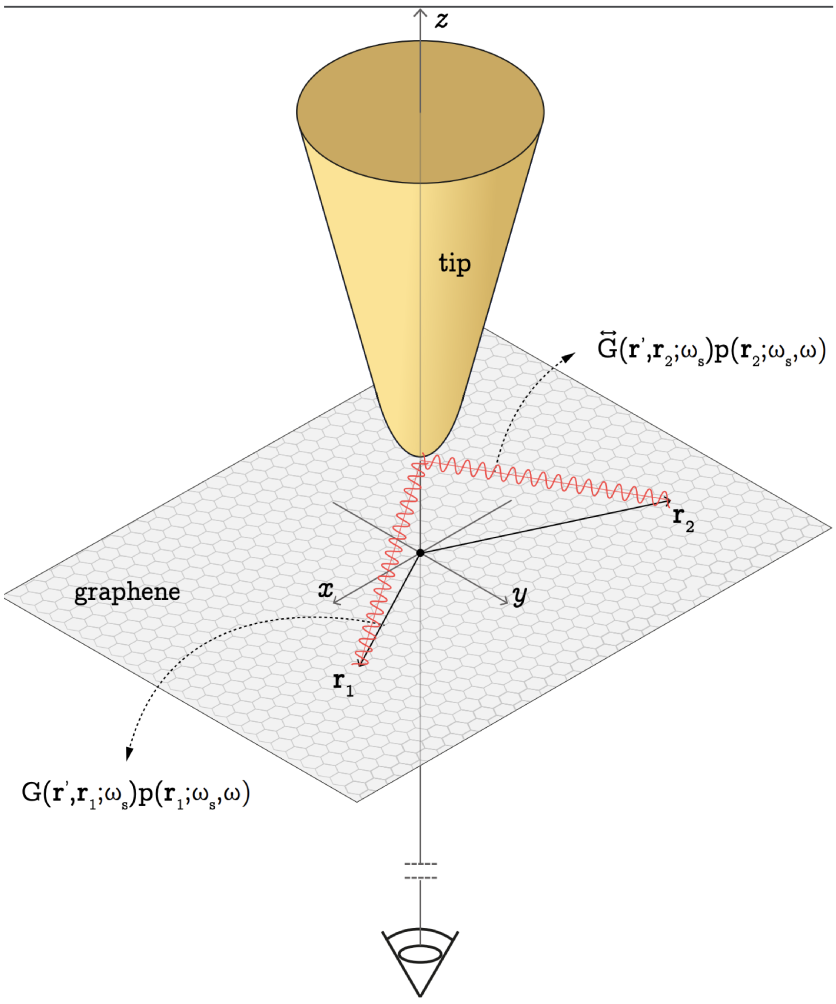

Figure 3.1: System of Reference
Spatial distribution of the three components of the TERS model: The nanoantenna's tip is located in $\mathbf{r}' = (0,0,z)$; the graphene is located in the $xy\text{-}plane$ $(x,y,0)$ and the detector located far from the scattering region in $\mathbf{r}_0$. The red waves represent the light scattered from points $\mathbf{r} = \mathbf{r}_1$ and $\mathbf{r} = \mathbf{r}_2$ propagating to the point $\mathbf{q} = \mathbf{r}'$. These two waves might interfere if $|\mathbf{r}_1 - \mathbf{r}_2| \leq L_c$. Adapted from Ref. [29].

$$\mathbf{E}^s(\mathbf{q};\omega) = \frac{\omega_s^2}{\epsilon_0 c^2} \int_{\mathbb{D}} d^2 r \overleftrightarrow{G}(\mathbf{q},\mathbf{r};\omega)\mathbf{p}(\mathbf{r};\omega), \tag{3.1}$$

where constants ϵ_0 and c are the vacuum's permittivity and the speed of light, respectively. Each dipole can be written in terms of its polarizability tensor $\overleftrightarrow{\alpha}(\mathbf{r};\omega)$ and an excitation electric field $\mathbf{E}(\mathbf{r};\omega)$:

$$\mathbf{p}(\mathbf{r};\omega) = \overleftrightarrow{\alpha}(\mathbf{r};\omega)\mathbf{E}(\mathbf{r};\omega) \tag{3.2}$$

3.1.2 Detector

The detector is positioned at $\mathbf{r}_0$, infinitely distant from the scattered region. The detector is able to measure the intensity associated with of the scattered electric field $\mathbf{E}^s(\mathbf{r}_0, \omega_s)$. Only the Raman frequency ω_s is detected. This is the same as assuming that a filter is placed in front of the detector and is able to block all the photons except the ones of frequency ω_s. Then, the detector measures a signal of intensity $I(\mathbf{r}_0, \omega_s)$ which can be calculated as an ensemble average of $\mathbf{E}^s(\mathbf{r}_0, \omega_s)$ in the form

$$I(\mathbf{r}_0, \omega_s) = \langle \mathbf{E}^{s*}(\mathbf{r}_0, \omega_s) \cdot \mathbf{E}^s(\mathbf{r}_0, \omega_s) \rangle \,. \tag{3.3}$$

Inserting Eq.3.1 and 3.2 into 3.3 leads to

$$\begin{aligned} I(\mathbf{r}_0, \omega_s) &= \langle \mathbf{E}^{s*}(\mathbf{r}_0, \omega_s) \cdot \mathbf{E}^s(\mathbf{r}_0, \omega_s) \rangle \\ &= \frac{\omega_s^4}{\epsilon_0^2 c^4} \int_{\mathbb{D}} d^2 r_1 \int_{\mathbb{D}} d^2 r_2 \\ &\left\langle \overleftrightarrow{G}(\mathbf{r}_0, \mathbf{r}_1; \omega_s) \mathbf{p}(\mathbf{r}_1; \omega_s) \cdot \overleftrightarrow{G}(\mathbf{r}_0, \mathbf{r}_2; \omega_s) \mathbf{p}(\mathbf{r}_2; \omega, \omega_s) \right\rangle . \end{aligned} \tag{3.4}$$

The integrals are evaluated over the sample's domain.

3.1.3 Graphene

Redefining Eq.3.2 in terms of the graphene Raman tensor $\overleftrightarrow{\alpha}^{\gamma}$ describing the symmetry properties of a given mode γ excited by an electric field $\mathbf{E}(\mathbf{r}, \omega)$, leads to

$$\mathbf{p}^{\gamma}(\mathbf{r}; \omega_s, \omega) = \overleftrightarrow{\alpha}^{\gamma}(\mathbf{r}; \omega) \mathbf{E}(\mathbf{r}; \omega). \tag{3.5}$$

For the main modes observed in graphene, the $\overleftrightarrow{\alpha}^{\gamma}$ assume the values below (or a linear combination of them [70]) depending on the associated phonon symmetry [71]

$$\overleftrightarrow{\alpha}^{G}(E_{2g1}) = \alpha^{G} \begin{bmatrix} 1 & 0 \\ 0 & -1 \end{bmatrix}, \qquad \overleftrightarrow{\alpha}^{G}(E_{2g2}) = \alpha^{G} \begin{bmatrix} 0 & 1 \\ 1 & 0 \end{bmatrix}, \qquad \overleftrightarrow{\alpha}^{D,G'}(A_1) = \alpha^{D,G'} \begin{bmatrix} 1 & 0 \\ 0 & 1 \end{bmatrix}. \tag{3.6}$$

We have only considered the in-plane polarizability components because it is well established that graphene does not scatter efficiently for incoming or outgoing light polarized out-of-plane.

The total field $\mathbf{E}$ that excites the graphene results from the summation of incident electric field $\mathbf{E}_0$ and the electric field resulting from the interaction of the incident electric field and the nanoantenna. Before explicitly writing an equation for $\mathbf{E}$ in terms of the nanoantenna

scattered field and $\mathbf{E}_0$, another important phenomenon must be considered in the calculation of I: the coherence effects of the graphene phonons, as mentioned in the Sec.1.2. These interference is considered to happen within a Gaussian correlation of length L_c on the form [29]

$$\begin{aligned} I(\mathbf{r}_0, \omega_s) &\propto \langle \alpha^{*\gamma}(\mathbf{r}_1, \omega_s)\alpha^{\gamma}(\mathbf{r}_2, \omega_s)\rangle \\ &= \alpha^{*\gamma}(\mathbf{r}_1, \omega_s)\alpha^{\gamma}(\mathbf{r}_2, \omega_s)\frac{e^{-|\mathbf{r}_1-\mathbf{r}_2|^2/L_c}}{\pi L_c^2} \end{aligned} \tag{3.7}$$

In the next subsection, the interaction of $\mathbf{E}_0$ with the nanoantenna is addressed.

3.1.4 Nanoantenna

The total electric field $\mathbf{E}$ that excites the graphene can be calculated as

$$\mathbf{E}(\mathbf{r}, \omega) = \mathbf{E}_0(\mathbf{r}, \omega) + \frac{\omega_s^2}{\epsilon_0 c^2}\int_{tip} d^2r' \overleftrightarrow{G}^0(\mathbf{r}, \mathbf{r}'; \omega_s)\overleftrightarrow{\alpha}_{tip}(\mathbf{r}'; \omega)\mathbf{E}_0(\mathbf{r}'; \omega) \tag{3.8}$$

where the first term is simply the incident electric field and the second one is the secondary dipole field generated by the nanoantenna excited by $\mathbf{E}_0$, where α_{tip} is the nanoantenna's polarizability tensor. In order to evaluate the integral, two simplifications concerning the nanoantenna's properties can be considered, as in Ref. [23]. The first one comes from the anisotropic polarizability of the nanoantenna

$$\overleftrightarrow{\alpha}(\mathbf{r}') = \begin{bmatrix} \alpha_\perp & 0 & 0 \\ 0 & \alpha_\perp & 0 \\ 0 & 0 & \alpha_\parallel \end{bmatrix} \tag{3.9}$$

where

$$\alpha_\parallel = 2\pi\epsilon_0 r_{tip}^3 f_e(\omega) \tag{3.10}$$

$$\alpha_\perp = 4\pi\epsilon_0 r_{tip}^3 \frac{\epsilon(\omega) - 1}{\epsilon(\omega) + 2}. \tag{3.11}$$

Since the component of $\mathbf{E}_0$ along the z direction is the most important one, the contributions from the $\alpha_\perp$ terms are neglected.

The second consideration states that the entire contribution of the nanoantenna (integral over the tips surface) can be approximated as a single dipole located at $\mathbf{r}' = (0, 0, z)$, leading to a trivial integration over a single point. Therefore, Eq.3.8 can be rewritten as

$$\mathbf{E}(\mathbf{r},\omega) = \mathbf{E}_0(\mathbf{r},\omega) + \frac{\omega_s^2}{\epsilon_0 c^2}\overleftrightarrow{G}^0(\mathbf{r},z;\omega)\overleftrightarrow{\alpha}_{tip}(z;\omega)\mathbf{E}(z;\omega). \tag{3.12}$$

3.1.5 Scattering modes

In the same way that **E** takes into account the nanoantenna's effects, the Green's function in Eq.3.4 also does. It can be written in terms of the nanoatenna's components as

$$\overleftrightarrow{G}(\mathbf{r}_0,\mathbf{r};\omega_s) = \overleftrightarrow{G}^0(\mathbf{r}_0,\mathbf{r};\omega_s) + \frac{\omega_s^2}{\epsilon_0 c^2}\overleftrightarrow{\overleftrightarrow{G}}^0(\mathbf{r}_0,\mathbf{r};\omega_s)\overleftrightarrow{\alpha}_{tip}(z;\omega_s)\overleftrightarrow{G}^0(z,\mathbf{r};\omega_s). \tag{3.13}$$

The first term in the right-hand side accounts for the for the field that propagates directly to the detector. The second accounts for the scattered modes generated by multiple scattering events between the graphene and the nanoantennas's tip.

By grouping all elements introduced up to now, Eq.3.4 can finally be rewritten in a matrix representation form as:

$$\begin{aligned} I(\mathbf{r}_0,\omega_s) =& \frac{\omega_s^4}{\epsilon_0^2 c^4}\sum_{l,m,n}\sum_{i,j}\iint_{-\infty}^{\infty} dx_2 dy_2 G_{ln}(-z_\infty;x_2,y_2;\omega_s)\alpha_{nj}^{\gamma}E_j(x_2,y_2,\omega) \\ &\times \iint_{-\infty}^{\infty} dx_1 dy_1 \frac{e^{[(x_1-x_2)^2+(y_1-y_2)^2]/Lc^2}}{\pi L c^2} G_{lm}^*(-z_\infty;x_2,y_2;\omega_s)\alpha^{\gamma *}E_i^*(x_1,y_1,\omega). \end{aligned} \tag{3.14}$$

The introduction of the terms derived in 3.1.3 and 3.1.4 gives

$$\begin{aligned} G_{ln}(-z_\infty;x_2,y_2;\omega_s)\alpha_{nj}^{\gamma}E_j(x_2,y_2,\omega) =& \; G_{ln}^0(-z_\infty;x,y;\omega_s)\alpha_{nj}^{\gamma}(x,y,\omega)E_{0j}(x,y;\omega) \\ &+ \frac{\omega_s^2}{\epsilon_0 c^2}G_{lz}^0(-z_\infty;z';\omega_s)\alpha_{\parallel}(\omega_s)G_{zn}^0(z';x,y;\omega_s)\alpha_{nj}^{\gamma}(x,y;\omega)E_{0j}(x,y;\omega) \\ &+ \frac{\omega_s^2}{\epsilon_0 c^2}G_{ln}^0(-z_\infty;x,y;\omega_s)\alpha_{nj}^{\gamma}(x,y;\omega)G_{jz}^0(x,y;z';\omega)\alpha_{\parallel}(\omega)E_{0j}(x,y,\omega) \\ &+ \frac{\omega^2}{\epsilon_0 c^2}G_{ln}^0(-z_\infty;z';\omega_s)\alpha_{\parallel}(\omega_s)G_{zn}(z';x,y;\omega_s)\alpha_{nj}^{\gamma}(x,y;\omega) \\ &\times G_{jz}^0(x,y;z';\omega)\alpha_{\parallel}E_{0z}(z';\omega) \end{aligned} \tag{3.15}$$

The first term corresponds to the *S* mode, which is related to the conventional Raman far-field scattering; it has no relation with any nanoantenna's component whatsoever. The second term accounts for the photons scattered by the nanoantenna and subsequently scattered

by the graphene, namely ST. The third one inverts this order, TS: first the graphene scattering and then the nanoantenna. Finally, the last term is the light scattered from the tip to the graphene, and then back the nanoantenna, TST.

The S mode and the TS mode are assumed here to be orders of magnitude weaker than the TST and ST modes, and they will be neglected in the present work, following the procedure of Ref. [29].

3.1.6 The Simplified Tip-approach equation

After taking care of all the assumptions and considerations explained in the last subsections, the integral is tricky and requires taking Fourier transformation and approximations. The calculation can be implemented in a $Mathematica$ environment, but for a better understanding of how the experimental parameters play a role, the result can be evidenced in a simplified on the form equation [48]

$$I_{\Gamma}^{TERS}(\Delta z) = C_{\Gamma} f_e^2 r_{tip}^6 \left(f_e^2 r_{tip}^6 g_{\Gamma}^{TST}(L_c, z) + g_{\Gamma}^{ST}(L_c, z) \right) \tag{3.16}$$

Here we just want to stretch out that I_{Γ}^{TERS} has two contributions: the functions g^{TST} and g^{ST} related to the scattering modes TST and ST, respectively. C_{Γ} accounts for the Raman cross section of the Γ symmetry mode and several other factor not explicitly considered in this formulation, such as detector's sensitivity, laser intensity and system alignment.

Equation 3.16 already brings the important ingredients for describing the relation between the tip-approach curve and the experimental parameters of interest, including f_e. In order to get a better understanding of Eq.3.16 and how to use it in a protocol to determine f_e, it is important to understand how Γ, L_c, r_{tip} and f_e influence the tip-approach curve. The next section will be dedicated to some results.

3.2 Study of the parameters

For studying the Γ and L_c influence on $I_{\Gamma}^{TERS}(\Delta z)$, consider the fixed the parameters $f_e = 5$, $r_{tip} = 15nm$ and $z_0 = 3nm$ (see Table 3.1). Figs. 3.2a,b show the graphs for different symmetry modes mixing the A_{1g} and E_{2g} symmetries for a fixed value of $L_c = 30nm$. These symmetries were chosen to simulate the results from graphene, where the Raman peaks G and G' bands are related to the E_{2g} and A_{1g} symmetry modes, respectively [70]. Fig. 3.2a shows the absolute $I_{\Gamma}^{TERS}(\Delta z)$ in a log-log plot for $C_{\Gamma} = 1$. In Fig. 3.2b the same result is displayed but normalized at $\Delta z = 0$.

In the normalized picture, the faster the decay of the intensity as Δz increases, the larger the effective enhancement. The A_{1g} mode exhibits the larger enhancement, in agreement with [28, 29, 70]. Now, fixing the symmetry mode and varying the L_c, using the same tip

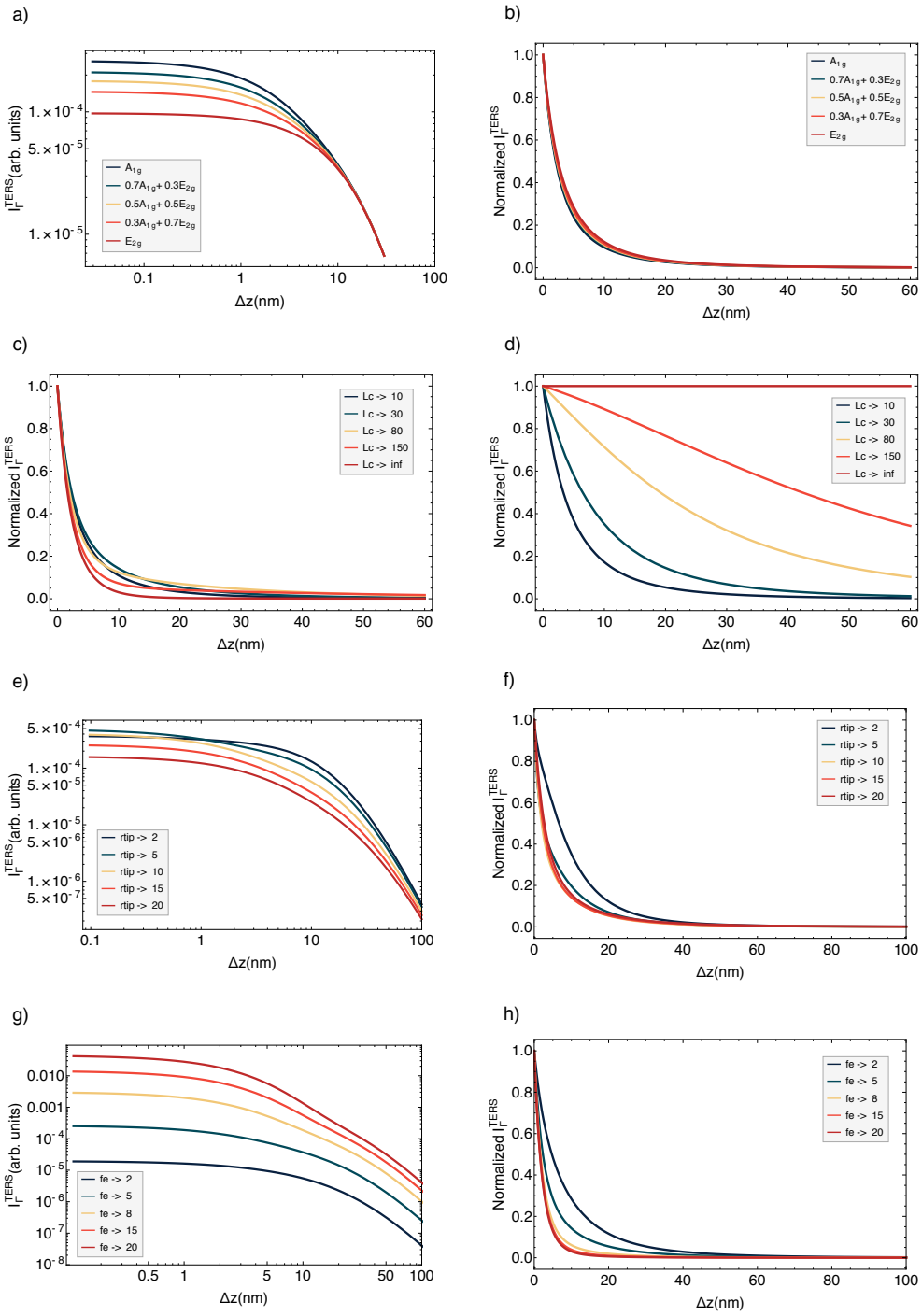

Figure 3.2: All graphics represent the tip-approach curves - $I_{\Gamma}^{TERS}(\Delta z)$ as a function of tip-displacement Δz. In each graph, one parameter is variable and all other parameters fixed, as summarized in Table 3.1. (a, e, g) are log-log plots, while the others exhibit a linear scale and are normalized. The normalization process consists in dividing each curve by its value at $\Delta z = 0$. Results first published in Ref. [48]

parameters as in Fig. 3.2a,b, Figs.3.2c and 3.2d show the tip-approach curves for the A_{1g} and E_{2g} symmetry modes, respectively (parameters summarized in Table 3.1). For the A_{1g} mode (G band), Fig. 3.2c, from $L_c \rightarrow 0$ to $L_c = 80nm$, indicated by the dark-blue line and yellow lines, respectively, the dependence with Δz are smother, showing that the ST scattering mode plays a more important role in these scattering events. By increasing the L_c value further, represented by the orange and red lines, the curves changes their behavior with Δz, decaying faster for smaller values of Δz , showing that the TST mode is more relevant after L_c values between 30 and 80nm, tending to the red curve for $L_c \rightarrow \infty$.

Fig. 3.2d shows the same plot for the E_{2g} mode. Again, the slope of the curves indicates that the ST scattering gets more relevant for larger values of L_c. For $L_c \rightarrow \infty$, the curve approaches to a constant value, indicating no tip-induced enhancement for the fully coherent E_{2g} scattering due to destructive interference, in agreement with [28, 29, 70].

The theory described in this section can now be used in a protocol to estimate f_e. It is crucial to have the z_0 and r_{tip} values well established and the sample properties L_c and Γ well defined. For this reason, it is important to have a reference material. To avoid the instrumental aspects hidden in C_Γ, it is also important to work with the normalized data. After a normalized tip-approach curve data is extracted from such a reference material, the protocol includes adjusting the data by choosing the value of f_e that better describes the normalized $I_\Gamma^{TERS}(\Delta z)$ curve. A graphene device is proposed here for the reference material because graphene is a widely studied 2D material [72] with a well-established L_c [28].

Table 3.1: Parameters used to plot the graphics in Fig.02

Panel	Scale	Fixed parameters	emphasized parameter
a)	Log-log	f_e = 5 r_{tip} = 15 nm z_0 = 3 nm L_c = 30 nm	phonon symmetry Γ
b)	Linear	f_e = 5 r_{tip} = 15 nm z_0 = 3 nm L_c = 30 nm	phonon symmetry Γ
c)	Linear	f_e = 5 r_{tip} = 15 nm z_0 = 3 nm $\Gamma = A_{1g}$	phonon coherence length L_c
d)	Linear	f_e = 5 r_{tip} = 15 nm z_0 = 3 nm $\Gamma = E_{2g}$	phonon coherence length L_c
e)	Log-log	f_e = 5 z_0 = 3 nm L_c = 30 nm $\Gamma = A_{1g}$	tip apex radius r_{tip}
f)	Linear	f_e = 5 z_0 = 3 nm L_c = 30 nm $\Gamma = A_{1g}$	tip apex radius r_{tip}
g)	Log-log	r_{tip} = 15 nm z_0 = 3 nm L_c = 30 nm $\Gamma = A_{1g}$	enhancement factor f_e
h)	Linear	r_{tip} = 15 nm z_0 = 3 nm L_c = 30 nm $\Gamma = A_{1g}$	enhancement factor f_e

Chapter 4

The Calibration Device and Measurement Protocol

The proposed protocol to measure the intrinsic enhancement factor f_e is described in this chapter. It is based on the fitting of the tip-approach curve $I_\Gamma^{TERS}(\Delta z)$ which depends on the tip-sample distance Δz. Figure 4.1 defines the relevant parameters. Considering the dipole located at the center of the sphere representing the tip apex, the total dipole-sample distance is given by $z = r_{tip} + z_0 + \Delta z$, where r_{tip} is the tip-apex sphere radius, and z_0 is the minimum distance achieved by the tip from the sample, as defined by the SPM setpoint. Γ and L_c are the phonon symmetry and coherence length, respectively.

The experimental data is acquired by measuring the Raman intensity S scattered by a graphene in a TERS system, for different tip-sample positions. Due to the difficulty and lack of standardized procedure to do this experiment, a calibration device is proposed to increase the reproducibility of the f_e determination.

In the following sections, the physics and mathematical aspects of tip-approach function $I_\Gamma^{TERS}(\Delta z)$ will be derived, followed by a study of the relevant parameters of both tip and sample that have an impact on the behavior of the curve, defining the calibration device. A referential material will be discussed as a standard material to measure f_e. Finally, the protocol itself will be described.

4.1 Fitting the Tip-approach Curves

The theory described in chapter 3 can now be used in a protocol to estimate f_e, as evidenced by the results displayed in Fig. 3.2. It is crucial to have the z_0 and r_{tip} values well established and the sample properties L_c and Γ well defined. For this reason, it is important to have a reference material. To avoid the instrumental aspects hidden in C_Γ, it is also important to work with the normalized data. After a normalized tip-approach curve data is extracted from such a reference material, the protocol includes adjusting the data by choosing the value of f_e

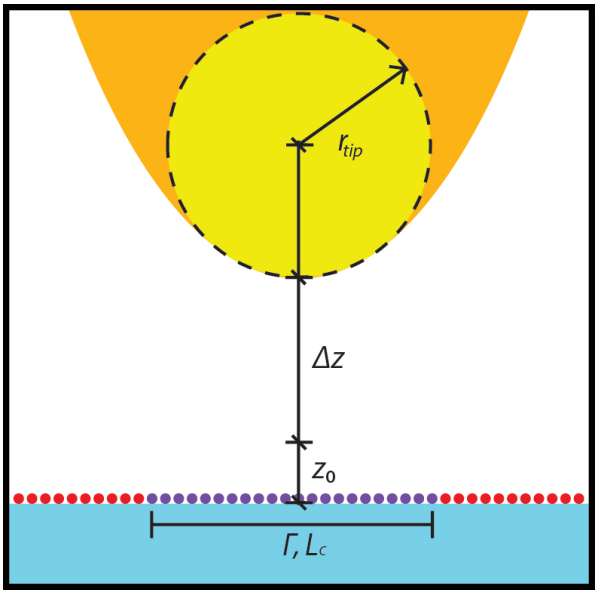

Figure 4.1: Tip-approach parameters diagram
Illustration of the relevant parameters for the definition of $I_\Gamma^{TERS}(\Delta z)$. The dipole excitation is located at the center of a sphere (yellow) with radius r_{tip}, at the apex of the nanoantenna (orange). The total dipole-sample distance is $z = z_0 + \Delta z + r_{tip}$, where Δz is the displacement from the initial setpoint z_0 in a tip-sample approach curve. The sample is represented by the small dots at the substrate on surface. Given a phonon with symmetry Γ, the light field scattered by the region smaller then the phonon coherence length L_c (purple dots) exhibits interference. Outside this region (red dots), the vibrations in the material system are uncorrelated. Image first published in Ref. [48]

that better describes the normalized $I_\Gamma^{TERS}(\Delta z)$ curve. A graphene-based callibration device is proposed here, because graphene is a widely studied 2D material [72] with a well-defined L_c [28].

4.2 Calibration Device

A few parameters have to be calibrated in a TERS system in order to be able to obtain the best performance of a nanoantenna. These parameters influence the accuracy of the Raman spectral frequencies, spectral imaging and scanning probe imaging. The proposed calibration device consists of a device that helps on these calibrations (see Fig. 4.2). The same platform can then be used to obtain f_e and, subsequently, to perform repeatable or traceable TERS experiments *in situ*. The components of the calibration device are described in Fig. 4.2, which comprises:

- **Substrate**: The substrate has to be a material with no optical response in the same range of a graphene Raman scatter. Glass, fused quartz or other transparent media are ideal for sample illumination from the bottom.

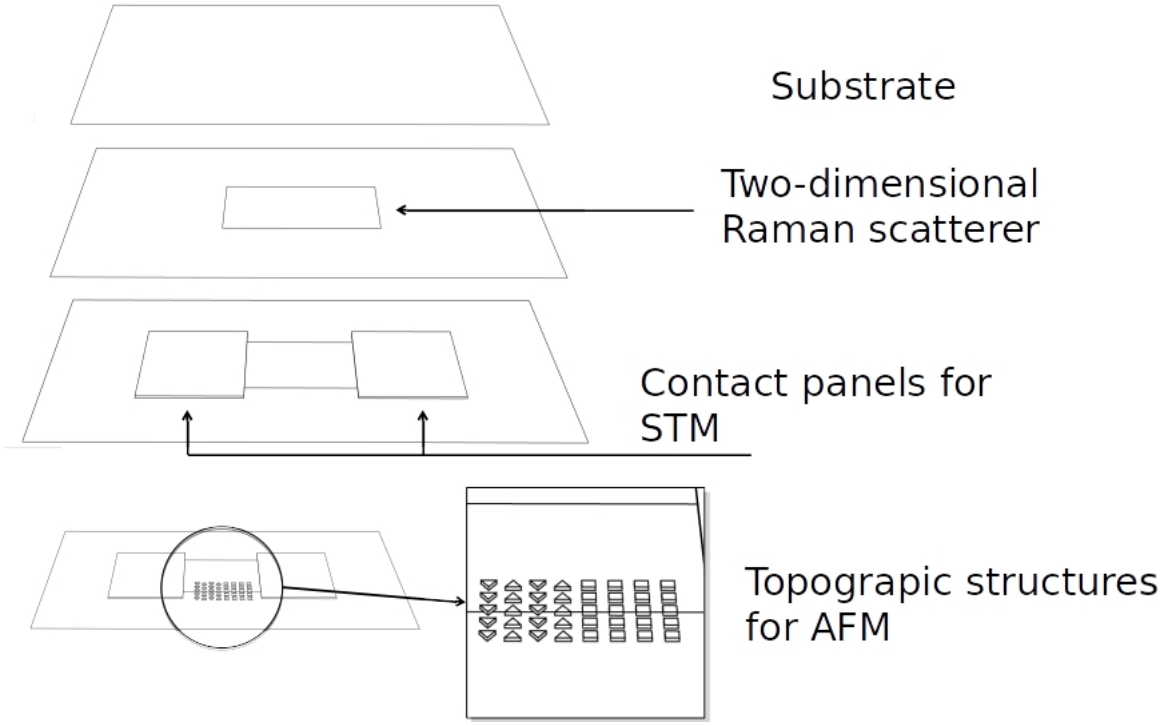

Figure 4.2: Schematics illustrates the TERS calibration device
Adapted from [48] and [73]. From top to bottom: 1) Transparent substrate; 2) Pristine monolayer graphene; 3) Contact panels made with conducting material for STM; 4) Topographic structures with different geometries for AFM calibration with well-defined edges.

- **Two-dimensional Raman scatterer**: graphene is the reference material utilized for confocal and TERS calibration.
- **Contact panels for STM**: in the case SPM is utilized in the STM mode, for current drain.
- **Topographic arrangement for AFM**: periodic topographic structure with well-defined dimensions for calibration of the SPM system in the AFM mode.

4.3 Experimental Protocol

4.3.1 Alignment of Scanning Confocal Optical Microscope

The scanning confocal optical microscope (SCOM) is the first system to be aligned and, in order to do that, it is ideal to have a sample that provides a strong Raman signal, with well-defined topological edges. This alignment is performed by moving the laser beam in and out of this reference material to maximize the optical lateral (X/Y) resolution (Fig.4.3).

The proposed platform provides a single layer graphene for the alignment of the SCOM system. Graphene is considered a reference material for this step, due to its strong

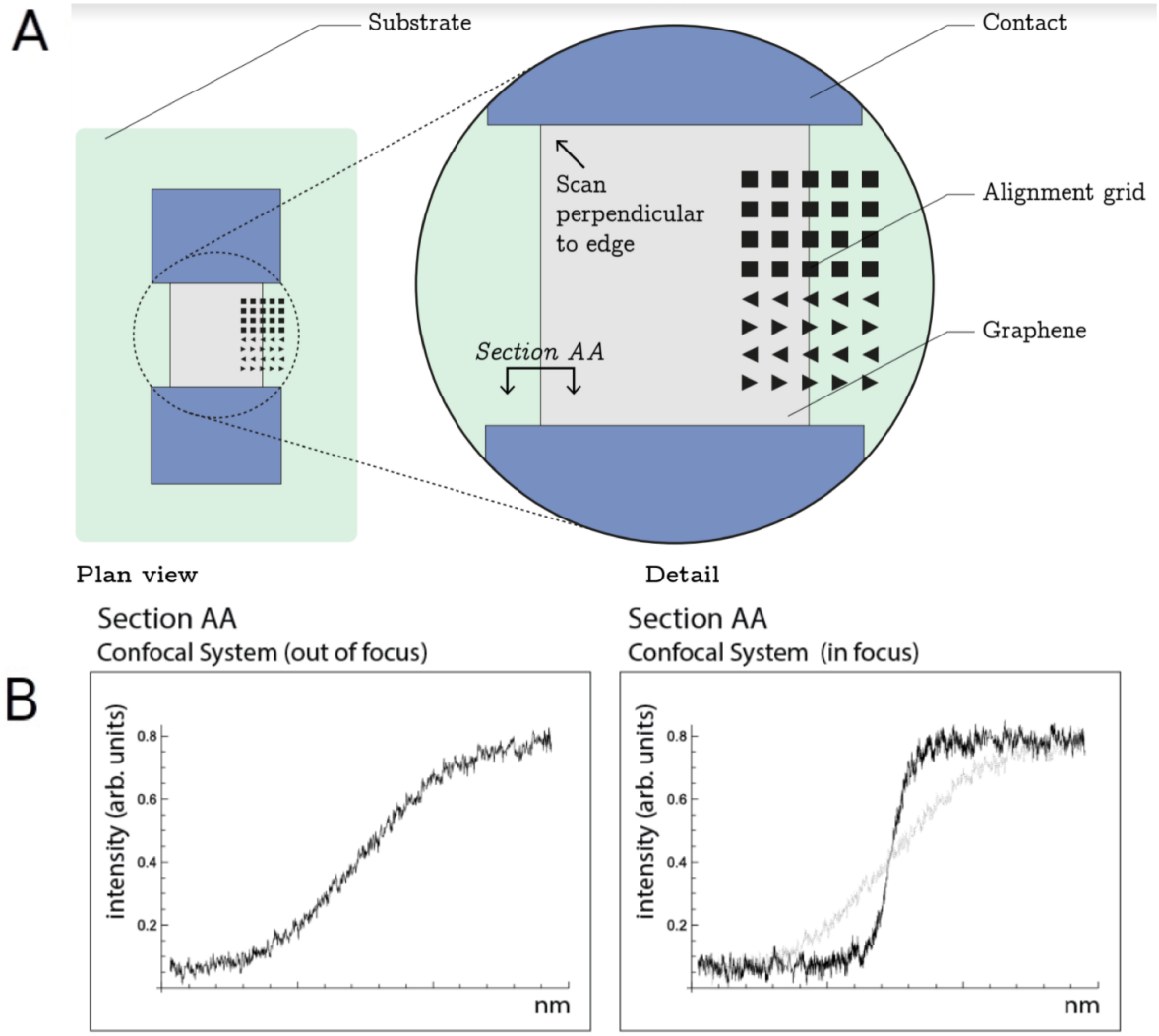

Figure 4.3: Schematics of the calibration device
Adapted from [48] and [73] The detailed view of A illustrates how the lateral scan must be performed to maximize the SNOM lateral resolution. B illustrates a misaligned system before calibration (left) and the expected signal after alignment in comparison with the first (right).

Raman signal and because it is a truly bidimensional (one atom thick) structure. By scanning in and out of the graphene sheet, the user is able to maximize the lateral resolution. This can be directly observed through the slope of the signal generated when the laser moves in and out of the graphene sheet. The steeper the slope, the better the optical lateral resolution of the system (Fig. 4.3B). The expected resolution for a good, well-aligned optical system is below half the wavelength of the excitation laser being used.

4.3.2 Configuration of Scanning Probe Optical Microscope

With the SCOM aligned, the second step is to configure the scanning probe optical microscopy (SPOM) system. The requirement in this step is to align the tip apex with the laser

focal point. The proposed platform provides a topographic alignment grid designed not only to facilitate this task (see Fig.4.4), but also to allow a quick and effective in-situ inspection of the tip apex radius.

To provide meaningful information for tip alignment, the grid has both square and triangular shapes. By using the triangular shapes as reference for alignment, it is possible to have relative tip-focus position information along both X and Y directions while scanning only in one direction (Fig. 4.4). By scanning over the topographic grid and comparing the generated confocal and topographical images, the user can see how misaligned the tip is with respect to the focal point, and to adjust the tip position in real time. The geometrical nature of the topographic grid facilitates the alignment procedure, by providing the user an easy way to calculate the tip-to-focus offset direction and distance.

In addition, this procedure can be used to evaluate the r_{tip}. This parameter is crucial to minimize the error in estimating the f_e by fitting the tip-approach curve.

4.3.3 Tip-approach Procedure

After the alignment of both SCOM and SPOM using this protocol, and having the r_{tip} characterized by the tip lateral resolution, the next step is finally the determination of f_e for a given phonon mode Γ.

The tip-approach curve consists in measuring the Raman Intensity $I_{\Gamma}^{TERS}(\Delta z)$ for different Δz values in the same XY position of the reference standard material (on top of graphene). The experimentally obtained $I_{\Gamma}^{TERS}(\Delta z)$ is then fit with the model described in chapter 3, using *Mathematica* (see APPENDIX A).

The absolute I_{Γ}^{TERS} values depend on the defined C_{Γ}, which includes environment aspects, such as distance to the detector. To eliminate this factor from our analysis, the signal should be normalized. All points must be divided by the Raman intensity obtained at $\Delta z = 0$. The f_e value is the one that better adjusts the tip-approach curves.

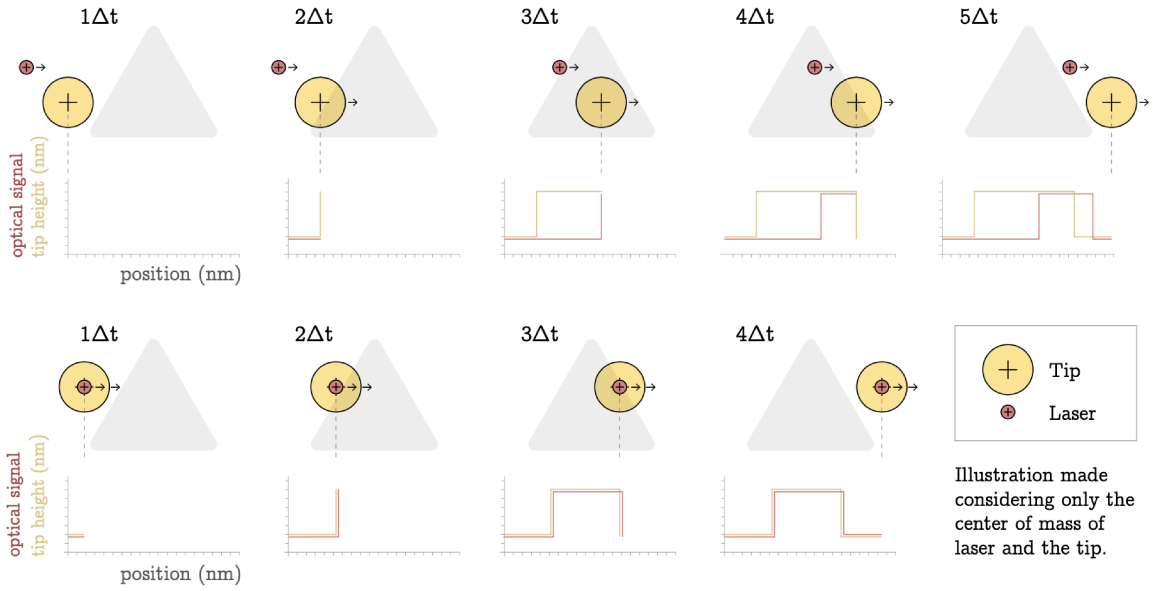

Figure 4.4: Scanning of a topographic structure

Adapted from [48] and [73] This figure illustrates the scanning of topographic structure (gray triangle), considering (top) the situation when the tip SPM (yellow circle) is misaligned with the laser spot (red circle), and (bottom) the situation when the tip and optical signal are aligned. The expected measured line profiles are below the figures. For the AFM tip, it is a measure of the tip height as a function of the lateral position. For the optics, it represents the measured signal intensity as function of the lateral position. By measuring both optical signal and tip-height as a function of the lateral movement, it is possible to infer whether the tip is aligned with the optical signal in the XY plane.

Chapter 5

Conclusion

As described in the Nanoantenna Fabrication subsection, there are several methods of producing nanoantennas. Currently, the definition of enhancement factor EF varies between different research groups, making it hard to access whether a tip is better than another. The protocol and calibration device described here intend to solve this problem. It is based on previous work that considers the nanoantennas intrinsics enhancement factor f_e, see Chap.3, and it can be inferred by adjusting a tip-approach curve, as detailed in Chap.4.

The parameters influencing the tip-approach curve shape were discussed in Sec.3.2 and summarized in Fig 3.2. Both sample properties, Γ and L_c, and tip properties r_{tip} and f_e, influence the behavior of the tip-approach curve. In order to measure the f_e, the parameters Γ, L_c and r_{tip}, must be measured. Therefore, the calibration device described in Sec.4.2 is a graphene-based device with well-defined Γ and L_c, to check r_{tip} and check the whole alignment of the system, by following the experimental protocol also described in Sec.4.2.

The methodology presented in this dissertation has already been used TERS community. The First one is the *Vasconcelos et al.* article (Ref. [42]). There the authors show a new method of fabricating nanopyramid-shaped tip with tunable LSPR conditions. In order to access the f_e of these tips, this protocol was followed resulting in a $f_e \approx 9$. This value is easily comparable with the result from Ref. [28] that found $f_e \approx 4$ for a nanoantenna made using another fabrication process.

The second contribution was to *Alencar et al.* (Ref. [74]). The main goal of the article was to infer the L_c of GaS using similar procedure. In order to do so, the TS mode was included in the tip-approach curve (not part of this dissertation) and used to adjust experimental data obtained in a TERS experiment. It resulted in a measured $f_e \approx 3.5$ and the consistent $L_c \approx 64$.

With this dissertation, we hope to help minimizing the arbitrariness of the definition of f_e for a TERS nanoantenna, and to provide an useful guide to measure it, providing a value to compare nanoantennas by means of their enhancements, and also enabling deriving other properties of the material, such as L_c.

Bibliography

[1] Raoul M. Stöckle, Yung Doug Suh, Volker Deckert, and Renato Zenobi. Nanoscale chemical analysis by tip-enhanced Raman spectroscopy. *Chemical Physics Letters*, 318(1-3):131–136, 2000.

[2] Mark S. Anderson. Locally enhanced Raman spectroscopy with an atomic force microscope. *Applied Physics Letters*, 76(21):3130–3132, 2000.

[3] Norihiko Hayazawa, Yasushi Inouye, Zouheir Sekkat, and Satoshi Kawata. Metallized tip amplification of near-field Raman scattering. *Optics Communications*, 183(1):333–336, 2000.

[4] Bruno Pettinger, Bin Ren, Gennaro Picardi, Rolf Schuster, and Gerhard Ertl. Nanoscale probing of adsorbed species by tip-enhanced Raman spectroscopy. *Physical Review Letters*, 92(9):8–11, 2004.

[5] L G Cançado, A Jorio, A Ismach, E Joselevich, A Hartschuh, and L Novotny. Mechanism of Near-Field Raman Enhancement in One-Dimensional Systems. *Physical Review Letters*, 103(18):186101, 2009.

[6] René Böhme, Dana Cialla, Marc Richter, Petra Rösch, Jürgen Popp, and Volker Deckert. Biochemical imaging below the diffraction limit - probing cellular membrane related structures by tip-enhanced Raman spectroscopy (TERS). *Journal of Biophotonics*, 3(7):455–461, 2010.

[7] Denys Naumenko, Valentinas Snitka, Elena Serviene, Ingrida Bruzaite, and Boris Snopok. In vivo characterization of protein uptake by yeast cell envelope: Single cell AFM imaging and μ-tip-enhanced Raman scattering study. *Analyst*, 138(18):5371–5383, 2013.

[8] C. Budich, U. Neugebauer, J. Popp, and V. Deckert. Cell wall investigations utilizing tip-enhanced Raman scattering. *Journal of Microscopy*, 229(3):533–539, 2008.

[9] A. Rasmussen and V. Deckert. Surface- and tip-enhanced Raman scattering of DNA components. *Journal of Raman Spectroscopy*, 37(1-3):311–317, 2006.

[10] Regina Treffer, Xiumei Lin, Elena Bailo, Tanja Deckert-Gaudig, and Volker Deckert. Distinction of nucleobases - A tip-enhanced Raman approach. *Beilstein Journal of Nanotechnology*, 2(1):628–637, 2011.

[11] Samar Najjar, David Talaga, Léonard Schué, Yannick Coffinier, Sabine Szunerits, Rabah Boukherroub, Laurent Servant, Vincent Rodriguez, and Sébastien Bonhommeau. Tip-enhanced raman spectroscopy of combed double-stranded DNA bundles. *Journal of Physical Chemistry C*, 118(2):1174–1181, 2014.

[12] Dana Cialla, Tanja Deckert-Gaudig, Christian Budich, Michael Laue, Robert Möller, Dieter Naumann, Volker Deckert, and Jürgen Popp. Raman to the limit: Tip-enhanced Raman spectroscopic investigations of a single tobacco mosaic virus. *Journal of Raman Spectroscopy*, 40(3):240–243, 2009.

[13] Cui Fan, Zhiqiang Hu, Lela K. Riley, Gregory A. Purdy, Azlin Mustapha, and Mengshi Lin. Detecting food- and waterborne viruses by surface-enhanced raman spectroscopy. *Journal of Food Science*, 75(5):302–307, 2010.

[14] Peter Hermann, Antje Hermelink, Veronika Lausch, Gudrun Holland, Lars Möller, Norbert Bannert, and Dieter Naumann. Evaluation of tip-enhanced Raman spectroscopy for characterizing different virus strains. *Analyst*, 136(6):1148–1152, 2011.

[15] Tanja Deckert-Gaudig, Evelyn Kämmer, and Volker Deckert. Tracking of nanoscale structural variations on a single amyloid fibril with tip-enhanced Raman scattering. *Journal of Biophotonics*, 5(3):215–219, 2012.

[16] Boon Siang Yeo, Stefanie Mädler, Thomas Schmid, Weihua Zhang, and Renato Zenobi. Tip-enhanced Raman spectroscopy can see more: The case of cytochrome c. *Journal of Physical Chemistry C*, 112(13):4867–4873, 2008.

[17] Dmitry Kurouski, Thomas Postiglione, Tanja Deckert-Gaudig, Volker Deckert, and Igor K. Lednev. Amide i vibrational mode suppression in surface (SERS) and tip (TERS) enhanced Raman spectra of protein specimens. *Analyst*, 138(6):1665–1673, 2013.

[18] Y. Saito, M. Motohashi, N. Hayazawa, and S. Kawata. Stress imagining of semiconductor surface by tip-enhanced Raman spectroscopy. *Journal of Microscopy*, 229(2):217–222, 2008.

[19] Alvarado Tarun, Norihiko Hayazawa, and Satoshi Kawata. Tip-Enhanced Raman spectroscopy for nanoscale strain characterization. *Analytical and Bioanalytical Chemistry*, 394(7):1775–1785, 2009.

[20] Ryan Beams, Luiz Gustavo Cançado, Ado Jorio, A. Nick Vamivakas, and Lukas Novotny. Tip-enhanced Raman mapping of local strain in graphene. *Nanotechnology*, 26(17):1–6, 2015.

[21] Anatoly V. Zayats, Igor I. Smolyaninov, and Alexei A. Maradudin. Nano-optics of surface plasmon polaritons. *Physics Reports*, 408(3-4):131–314, 2005.

[22] Satoshi Kawata and Vladimir M. Shalaev. *Tip Enhancement*. Elsevier, 2007.

[23] Lukas Novotny and Bert Hecht. *Principles of Nano-Optics*, volume 91. Cambridge University Press, Cambridge, 2012.

[24] A. L. Demming, F. Festy, and D. Richards. Plasmon resonances on metal tips: Understanding tip-enhanced Raman scattering. *Journal of Chemical Physics*, 122(18), 2005.

[25] P. F. Liao and A. Wokaun. Lightning rod effect in surface enhanced Raman scattering. *The Journal of Chemical Physics*, 76(1):751–752, 1982.

[26] K. S. Youngworth and T. G Brown. Focusing of high numerical aperture cylindrical-vector beams. *Optics Express*, 7(2):77, 2000.

[27] Nastaran Kazemi-Zanjani, Sylvain Vedraine, and François Lagugné-Labarthet. Localized enhancement of electric field in tip-enhanced Raman spectroscopy using radially and linearly polarized light. *Optics Express*, 21(21):25271, 2013.

[28] Ryan Beams, Luiz Gustavo Cançado, Sang Hyun Oh, Ado Jorio, and Lukas Novotny. Spatial coherence in near-field Raman scattering. *Physical Review Letters*, 113(18):1–5, 2014.

[29] Luiz Gustavo Cançado, Ryan Beams, Ado Jorio, and Lukas Novotny. Theory of spatial coherence in near-field Raman scattering. *Physical Review X*, 4(3):1–14, 2014.

[30] Markus Pfeiffer, Boris V Senkovskiy, Danny Haberer, Felix R Fischer, Fan Yang, Klaus Meerholz, Yoichi Ando, Alexander Grüneis, and Klas Lindfors. Enhanced light–matter interaction of aligned armchair graphene nanoribbons using arrays of plasmonic nanoantennas. *2D Materials*, 5(4):045006, jul 2018.

[31] R. S. Alencar, Cassiano Rabelo, Hudson L.S. Miranda, Thiago L. Vasconcelos, Bruno S. Oliveira, Aroldo Ribeiro, Bruno C. Públio, Jenaina Ribeiro-Soares, A. G.Souza Filho, Luiz Gustavo Cançado, and Ado Jorio. Probing Spatial Phonon Correlation Length in Post-Transition Metal Monochalcogenide GaS Using Tip-Enhanced Raman Spectroscopy. *Nano Letters*, pages 7357–7364, 2019.

[32] M. Klein and G. Schwitzgebel. An improved lamellae drop-off technique for sharp tip preparation in scanning tunneling microscopy. *Review of Scientific Instruments*, 68(8):3099–3103, 1997.

[33] J. S. Lloyd, A. Williams, R. H. Rickman, A. McCowen, and P. R. Dunstan. Reproducible electrochemical etching of silver probes with a radius of curvature of 20 nm for tip-enhanced Raman applications. *Applied Physics Letters*, 99(14):1–4, 2011.

[34] J. Stadler, T. Schmid, and R. Zenobi. Nanoscale chemical imaging using top-illumination tip-enhanced Raman spectroscopy. *Nano Letters*, 10(11):4514–4520, 2010.

[35] Bin Ren, Gennaro Picardi, and Bruno Pettinger. Preparation of gold tips suitable for tip-enhanced Raman spectroscopy and light emission by electrochemical etching. *Review of Scientific Instruments*, 75(4):837–841, 2004.

[36] Thiago L. Vasconcelos, Bráulio S. Archanjo, Benjamin Fragneaud, Bruno S. Oliveira, Juha Riikonen, Changfeng Li, Douglas S. Ribeiro, Cassiano Rabelo, Wagner N. Rodrigues, Ado Jorio, Carlos A. Achete, and Luiz Gustavo Cançado. Tuning Localized Surface Plasmon Resonance in Scanning Near-Field Optical Microscopy Probes. *ACS Nano*, 9(6):6297–6304, 2015.

[37] Rebecca L. Agapov, Alexei P. Sokolov, and Mark D. Foster. Protecting TERS probes from degradation: Extending mechanical and chemical stability. *Journal of Raman Spectroscopy*, 44(5):710–716, 2013.

[38] Boon Siang Yeo, Thomas Schmid, Weihua Zhang, and Renato Zenobi. Towards rapid nanoscale chemical analysis using tip-enhanced Raman spectroscopy with Ag-coated dielectric tips. *Analytical and Bioanalytical Chemistry*, 387(8):2655–2662, 2007.

[39] Boon Siang Yeo, Weihua Zhang, Christophe Vannier, and Renato Zenobi. Enhancement of Raman signals with silver-coated tips. *Applied Spectroscopy*, 60(10):1142–1147, 2006.

[40] Timothy W. Johnson, Zachary J. Lapin, Ryan Beams, Nathan C. Lindquist, Sergio G. Rodrigo, Lukas Novotny, and Sang Hyun Oh. Highly reproducible near-field optical imaging with sub-20-nm resolution based on template-stripped gold pyramids. *ACS Nano*, 6(10):9168–9174, 2012.

[41] Nathan C. Lindquist, Prashant Nagpal, Antoine Lesuffleur, David J. Norris, and Sang Hyun Oh. Three-dimensional plasmonic nanofocusing. *Nano Letters*, 10(4):1369–1373, 2010.

[42] T.L. Vasconcelos, B.S. Archanjo, B.S. Oliveira, R. Valaski, R.C. Cordeiro, H.G. Medeiros, C. Rabelo, A. Ribeiro, P. Ercius, C.A. Achete, A. Jorio, and L.G. Cançado. Plasmon-Tunable Tip Pyramids: Monopole Nanoantennas for Near-Field Scanning Optical Microscopy. *Advanced Optical Materials*, 6(20), 2018.

[43] Chen Gong and Marina S. Leite. Noble Metal Alloys for Plasmonics. *ACS Photonics*, 3(4):507–513, 2016.

[44] Farshid Pashaee, Renjie Hou, Pierangelo Gobbo, Mark S. Workentin, and François Lagugné-Labarthet. Tip-enhanced Raman spectroscopy of self-assembled thiolated monolayers on flat gold nanoplates using gaussian-transverse and radially polarized excitations. *Journal of Physical Chemistry C*, 117(30):15639–15646, 2013.

[45] Rodolfo V Maximiano, Ryan Beams, Lukas Novotny, Ado Jorio, and Luiz Gustavo Cançado. Mechanism of near-field Raman enhancement in two-dimensional systems. *Physical Review B - Condensed Matter and Materials Physics*, 85(23):1–8, 2012.

[46] Zhilin Yang, Javier Aizpurua, and Hongxing Xu. Electromagnetic field enhancement in TERS configurations. *Journal of Raman Spectroscopy*, 40(10):1343–1348, 2009.

[47] Lingyan Meng, Tengxiang Huang, Xiang Wang, Shu Chen, Zhilin Yang, and Bin Ren. Gold-coated AFM tips for tip-enhanced Raman spectroscopy: theoretical calculation and experimental demonstration. *Optics Express*, 23(11):13804, 2015.

[48] Aroldo Ribeiro Neto, Cassiano Rabelo, Luiz Gustavo Cancado, Michael Engel, Mathias Steiner, and Ado Jorio. Protocol and reference material for measuring the nanoantenna enhancement factor in Tip-enhanced Raman Spectroscopy. *INSCIT 2019 - 4th International Symposium on Instrumentation Systems, Circuits and Transducers*, (3):1–6, 2019.

[49] Johannes Stadler, Thomas Schmid, and Renato Zenobi. Developments in and practical guidelines for tip-enhanced Raman spectroscopy. *Nanoscale*, 4(6):1856–1870, 2012.

[50] Naresh Kumar, Alasdair Rae, and Debdulal Roy. Accurate measurement of enhancement factor in tip-enhanced Raman spectroscopy through elimination of far-field artefacts. *Applied Physics Letters*, 104(12), 2014.

[51] D. Mehtani, N. Lee, R. D. Hartschuh, A. Kisliuk, M. D. Foster, A. P. Sokolov, F. Čajko, and I. Tsukerman. Optical properties and enhancement factors of the tips for apertureless near-field optics. *Journal of Optics A: Pure and Applied Optics*, 8(4), 2006.

[52] Dmitry S. Bulgarevich and Masayuki Futamata. Apertureless tip-enhanced Raman microscopy with confocal epi-illumination/collection optics. *Applied Spectroscopy*, 58(7):757–761, 2004.

[53] N. Jiang, E. T. Foley, J. M. Klingsporn, M. D. Sonntag, N. A. Valley, J. A. Dieringer, T. Seideman, G. C. Schatz, M. C. Hersam, and R. P. Van Duyne. Observation of multiple vibrational modes in ultrahigh vacuum tip-enhanced Raman spectroscopy combined with molecular-resolution scanning tunneling microscopy. *Nano Letters*, 12(10):5061–5067, 2012.

[54] Bert Voigtländer. Scanning Probe Microscopy: Atomic Force Microscopy and Scanning Tunneling Microscopy. *NanoScience and Technology*, 2015.

[55] D. Mehtani, N. Lee, R. D. Hartschuh, A. Kisliuk, M. D. Foster, A. P. Sokolov, and J. F. Maguire. Nano-Raman spectroscopy with side-illumination optics. *Journal of Raman Spectroscopy*, 36(11):1068–1075, 2005.

[56] Ute Neugebauer, Petra Rösch, Michael Schmitt, Jürgen Popp, Carine Julien, Akiko Rasmussen, Christian Budich, and Volker Deckert. On the way to nanometer-sized information of the bacterial surface by tip-enhanced Raman spectroscopy. *ChemPhysChem*, 7(7):1428–1430, 2006.

[57] Bruno PETTINGER, Gennaro PICARDI, Rolf SCHUSTER, and Gerhard ERTL. Surface Enhanced Raman Spectroscopy: Towards Single Molecule Spectroscopy. *Electrochemistry*, 68(12):942–949, dec 2000.

[58] Norikiko Hayazawa, Yasushi Inouye, Zouheir Sekkat, and Satoshi Kawata. Near-field Raman imaging of organic molecules by an apertureless metallic probe scanning optical microscope. *Journal of Chemical Physics*, 117(3):1296–1301, 2002.

[59] Norihiko Hayazawa, Alvarado Tarun, Yasushi Inouye, and Satoshi Kawata. Near-field enhanced Raman spectroscopy using side illumination optics. *Journal of Applied Physics*, 92(12):6983–6986, 2002.

[60] Bruno Pettinger, Gennaro Picardi, Rolf Schuster, and Gerhard Ertl. Surface-enhanced and STM-tip-enhanced Raman spectroscopy at metal surfaces. *Single Molecules*, 3(5-6):285–294, 2002.

[61] Norihiko Hayazawa, Takaaki Yano, Hiroyuki Watanabe, Yasushi Inouye, and Satoshi Kawata. Detection of an individual single-wall carbon nanotube by tip-enhanced near-field Raman spectroscopy. *Chemical Physics Letters*, 376(1-2):174–180, 2003.

[62] Bruno Pettinger, Bin Ren, Gennaro Picardi, Rolf Schuster, and Gerhard Ertl. Tip-enhanced Raman spectroscopy (TERS) of malachite green isothiocyanate at Au(111): Bleaching behavior under the influence of high electromagnetic fields. *Journal of Raman Spectroscopy*, 36(6-7):541–550, 2005.

[63] Christophe Vannier, Boon Siang Yeo, Jeremy Melanson, and Renato Zenobi. Multifunctional microscope for far-field and tip-enhanced Raman spectroscopy. *Review of Scientific Instruments*, 77(2), 2006.

[64] Katrin F. Domke, Dai Zhang, and Bruno Pettinger. Toward Raman fingerprints of single dye molecules at atomically smooth Au(111). *Journal of the American Chemical Society*, 128(45):14721–14727, 2006.

[65] Dai Zhang, Katrin F. Domke, and Bruno Pettinger. Tip-enhanced Raman spectroscopic studies of the hydrogen bonding between adenine and thymine adsorbed on Au (111). *ChemPhysChem*, 11(8):1662–1665, 2010.

[66] Jens Steidtner and Bruno Pettinger. High-resolution microscope for tip-enhanced optical processes in ultrahigh vacuum. *Review of Scientific Instruments*, 78(10), 2007.

[67] Jens Steidtner and Bruno Pettinger. Tip-enhanced Raman spectroscopy and microscopy on single dye molecules with 15 nm resolution. *Physical Review Letters*, 100(23):1–4, 2008.

[68] Marc Chaigneau, Gennaro Picardi, and Razvigor Ossikovski. Molecular arrangement in self-assembled azobenzene-containing thiol monolayers at the individual domain

level studied through polarized near-field raman spectroscopy. *International Journal of Molecular Sciences*, 12(2):1245–1258, 2011.

[69] Emil Wolf. Emil Wolf-Introduction to the Theory of Coherence and Polarization of Light-Cambridge University Press (2007).pdf, 2007.

[70] Ado Jorio, Niclas S. Mueller, and Stephanie Reich. Symmetry-derived selection rules for plasmon-enhanced Raman scattering. *Physical Review B*, 95(15):1–10, 2017.

[71] Ado Jorio, Riichiro Saito, Gene Dresselhaus, and Mildred S. Dresselhaus. *Raman Spectroscopy in Graphene Related Systems*. 2011.

[72] Ado Jorio. Raman Spectroscopy in Graphene-Based Systems: Prototypes for Nanoscience and Nanometrology. *ISRN Nanotechnology*, 2012(2):1–16, 2012.

[73] Steiner M. Jorio A. Rabelo C. Cançado L. G. Engel, M. and H. Miranda. Calibrating tip-enhanced raman microscopes, US20190383854A1.

[74] R.S. Alencar, C. Rabelo, H.L.S. Miranda, T.L. Vasconcelos, B.S. Oliveira, A. Ribeiro, B.C. Públio, J. Ribeiro-Soares, A.G.S. Filho, L.G. Cançado, and A. Jorio. Probing Spatial Phonon Correlation Length in Post-Transition Metal Monochalcogenide GaS Using Tip-Enhanced Raman Spectroscopy. *Nano Letters*, 2019.

Appendix A - Tip-approach curve fitting in *Mathematica*

In this Appendix it is shown the *Mathematica* implementation of the tip-approach curve and the fit process as part of the measurement protocol proposed in Chapter 4.

A.0.1 Numerical Solutions to Tip-approach Curve Intensities

The Eq.3.14 can be evaluated for G and G' modes and their associated phonon symmetries A_1, E_{2g1} and E_{2g2}, as well as for the scattering modes TST and ST, by solving the integral (38), (39), (51) and (52) of Ref. [29]. The *Mathematica* implementation of these four equation is written below:

```
a = .74;
b = 4;
c = .08;
d = 1.5;
ap = 0.78;
bp = 2.4;
cp = .18;
dp = .56;

hxx[z_]:=
(a/b^3 (2b - kx^2 z^2) Exp[-(kx^2 + ky^2) z^2 * (4b)^-1] + c/d^3 (2d - kx^2 z^2) Exp[-(kx^2 + ky^2) z^2 * (4d)^-1])
hxy[z_]:= (a/b^3 kxky z^2 Exp[-(kx^2 + ky^2) z^2 * (4b)^-1] + c/d^3 kxky z^2 Exp[-(kx^2 + ky^2) z^2 * (4d)^-1])

hyy[z_]:=
(a/b^3 (2b - ky^2 z^2) Exp[-(kx^2 + ky^2) z^2 * (4b)^-1] + c/d^3 (2d - ky^2 z^2) Exp[-(kx^2 + ky^2) z^2 * (4d)^-1])

hx[z_]:=kx (ap/bp^2 Exp[-(kx^2 + ky^2) z^2 / (4bp)] + cp/dp^2 Exp[-(kx^2 + ky^2) z^2 / (4dp)])

hy[z_]:=ky (ap/bp^2 Exp[-(kx^2 + ky^2) z^2 / (4bp)] + cp/dp^2 Exp[-(kx^2 + ky^2) z^2 / (4dp)])
```

```
fxxxx = Integrate[hxx[z] * hxx[z] * Exp[-(kx^2 + ky^2) Lc^2 / 4], {kx, -Infinity, Infinity},
{ky, -Infinity, Infinity}];

fxxyy = Integrate[hxx[z] * hyy[z] * Exp[-(kx^2 + ky^2) Lc^2 / 4], {kx, -Infinity, Infinity},
{ky, -Infinity, Infinity}];

fxyxy = Integrate[hxy[z] * hxy[z] * Exp[-(kx^2 + ky^2) Lc^2 / 4], {kx, -Infinity, Infinity},
{ky, -Infinity, Infinity}];

lxx = Integrate[hx[z] * hx[z] * Exp[-(kx^2) Lc^2 / 4], {kx, -Infinity, Infinity}]
```

$$
\begin{aligned}
fxxxx = {} & \frac{\text{“0.165318”}}{\text{“1.”}Lc^2+\text{“0.916667”}(rtip+z+z0)^2} + \frac{\text{“0.860168”}Lc^4}{\left(2Lc^2+(rtip+z+z0)^2\right)^3} + \\
& \frac{\text{“0.107521”}Lc^2(rtip+z+z0)^6}{\left(\text{“2.”}Lc^2+(rtip+z+z0)^2\right)^5} - \frac{\text{“0.0268803”}(rtip+z+z0)^8}{\left(\text{“2.”}Lc^2+(rtip+z+z0)^2\right)^5} + \\
& \frac{\text{“0.0635455”}}{\text{“1.”}Lc^2+\text{“1.33333”}(rtip+z+z0)^2} + \\
& (rtip + z + z0)^4 \\
& (\text{“0.000728675”}/ \\
& \left(\sqrt{\text{“0.0795775”}Lc^2 + \text{“0.072946”}(rtip + z + z0)^2}\right. \\
& \left.\left(\text{“0.25”}Lc^2 + \text{“0.229167”}(rtip + z + z0)^2\right)^{5/2}\right) + \\
& \text{“0.000746911”}/ \\
& \left(\sqrt{\text{“0.0795775”}Lc^2 + \text{“0.106103”}(rtip + z + z0)^2}\right. \\
& \left.\left(\text{“0.25”}Lc^2 + \text{“0.333333”}(rtip + z + z0)^2\right)^{5/2}\right) + \frac{\text{“0.322563”}Lc^4}{\left(2Lc^2+(rtip+z+z0)^2\right)^5} - \\
& \left.\frac{\text{“0.430084”}Lc^2}{\left(2Lc^2+(rtip+z+z0)^2\right)^4} + \frac{\text{“0.188162”}}{\left(2Lc^2+(rtip+z+z0)^2\right)^3}\right) + \\
& (rtip + z + z0)^2 \\
& (-(\text{“0.00534362”}/ \\
& \left(\sqrt{\text{“0.0795775”}Lc^2 + \text{“0.072946”}(rtip + z + z0)^2}\right. \\
& \left.\left.\left(\text{“0.25”}Lc^2 + \text{“0.229167”}(rtip + z + z0)^2\right)^{3/2}\right)\right) - \\
& \text{“0.00298764”}/ \\
& \left(\sqrt{\text{“0.0795775”}Lc^2 + \text{“0.106103”}(rtip + z + z0)^2}\right. \\
& \left.\left(\text{“0.25”}Lc^2 + \text{“0.333333”}(rtip + z + z0)^2\right)^{3/2}\right) - \frac{\text{“0.430084”}Lc^4}{\left(2Lc^2+(rtip+z+z0)^2\right)^4} + \\
& \left.\frac{\text{“0.645126”}Lc^2}{\left(2Lc^2+(rtip+z+z0)^2\right)^3}\right);
\end{aligned}
$$

$$
\begin{aligned}
fxyxy = {} & \\
& 2(rtip + z + z0)^4
\end{aligned}
$$

$$\left(\frac{\text{“0.0000525005”}}{\left(\text{“0.25”}Lc^2+\text{“0.125”}(rtip+z+z0)^2\right)^3}+\frac{\text{“0.000215257”}}{\left(\text{“0.25”}Lc^2+\text{“0.229167”}(rtip+z+z0)^2\right)^3}+\frac{\text{“0.000220644”}}{\left(\text{“0.25”}Lc^2+\text{“0.333333”}(rtip+z+z0)^2\right)^3}\right);$$

$$fxxyy = \text{“0.00112373”}\left(\left(\text{“299.346”}Lc^4+\text{“565.106”}Lc^2(rtip+z+z0)^2+\text{“240.94”}(rtip+z+z0)^4\right)/\left(\text{“1.”}Lc^6+\text{“2.75”}Lc^4(rtip+z+z0)^2+\text{“2.34722”}Lc^2(rtip+z+z0)^4+\text{“0.611111”}(rtip+z+z0)^6\right)+(rtip+z+z0)^2\left(-\left(\text{“1.68696”}/\left(\sqrt{\text{“0.0795775”}Lc^2+\text{“0.0397887”}(rtip+z+z0)^2}\left(\text{“0.25”}Lc^2+\text{“0.125”}(rtip+z+z0)^2\right)^{3/2}\right)\right)-\text{“4.75525”}/\left(\sqrt{\text{“0.0795775”}Lc^2+\text{“0.072946”}(rtip+z+z0)^2}\left(\text{“0.25”}Lc^2+\text{“0.229167”}(rtip+z+z0)^2\right)^{3/2}\right)-\text{“2.65868”}/\left(\sqrt{\text{“0.0795775”}Lc^2+\text{“0.106103”}(rtip+z+z0)^2}\left(\text{“0.25”}Lc^2+\text{“0.333333”}(rtip+z+z0)^2\right)^{3/2}\right)\right)+(rtip+z+z0)^4\left(\frac{\text{“5.98013”}}{\left(\text{“1.”}Lc^2+\text{“0.5”}(rtip+z+z0)^2\right)^3}+\frac{\text{“24.5191”}}{\left(\text{“1.”}Lc^2+\text{“0.916667”}(rtip+z+z0)^2\right)^3}+\frac{\text{“25.1327”}}{\left(\text{“1.”}Lc^2+\text{“1.33333”}(rtip+z+z0)^2\right)^3}\right)\right);$$

$$lxx = \frac{\text{“0.460876”}}{\left(\text{“1.”}Lc^2+\text{“0.833333”}(rtip+z+z0)^2\right)^2}+\frac{\text{“3.90696”}}{\left(\text{“1.”}Lc^2+\text{“2.20238”}(rtip+z+z0)^2\right)^2}+\frac{\text{“8.28005”}}{\left(\text{“1.”}Lc^2+\text{“3.57143”}(rtip+z+z0)^2\right)^2};$$

$$E2TST = rtip^6 fenh^2 \frac{9*rtip^6*fenh^2}{32*(z+rtip+z0)^8}\frac{1}{2}(fxxxx - fxxyy + 2fxyxy);$$

$$A1TST = rtip^6 fenh^2 \frac{9*rtip^6*fenh^2}{32*(z+rtip+z0)^8}(fxxxx + fxxyy);$$

$$E2ST = rtip^6 fenh^2 0.5lxx;$$

$$A1ST = rtip^6 fenh^2 0.5lxx;$$

A.0.2 TERS measurement Fit

In order to illustrate the fitting process, the data reported in published in [28] was fitted using the formulas derived in the previous subsection. It consists in Tip-approach curve for the graphene G'-band. The objective was to infer the f_e of the tip given the known parameters: $z_0 = 5nm$, $L_c = 33$ and $r_{tip} = 20$.

```
dadosPRLraw = Import["gp_center.txt", "Table"];

zdist = dadosPRLraw[[All,1]] − dadosPRLraw[[1,1]];
Gplist = dadosPRLraw[[All, 2]]/dadosPRLraw[[−1, 2]];
Gptable = Table[{(zdist[[i]]), Gplist[[i]]},{i,1,Length[zdist]}];


Model = ((A1TST + A1ST)/.{z0 → 5, Lc → 33, rtip → 20})/((A1TST + A1ST)/.{z0 → 5, Lc → 33,rti
GPRLfitgust = FindFit[Gptable,Model,{{fenh, 4}},z]

{fenh → "4.06411"}

Show[ListPlot[Gptable, PlotRange → All],
Plot[Evaluate[Model/.GPRLfitgust],{z,0,60}, PlotStyle → Directive[Thick,Red], PlotRange → All]]
```

As shown in Fig.A.1, the value f_e resulted from the fitting was 4.06, the same value reported in the article.

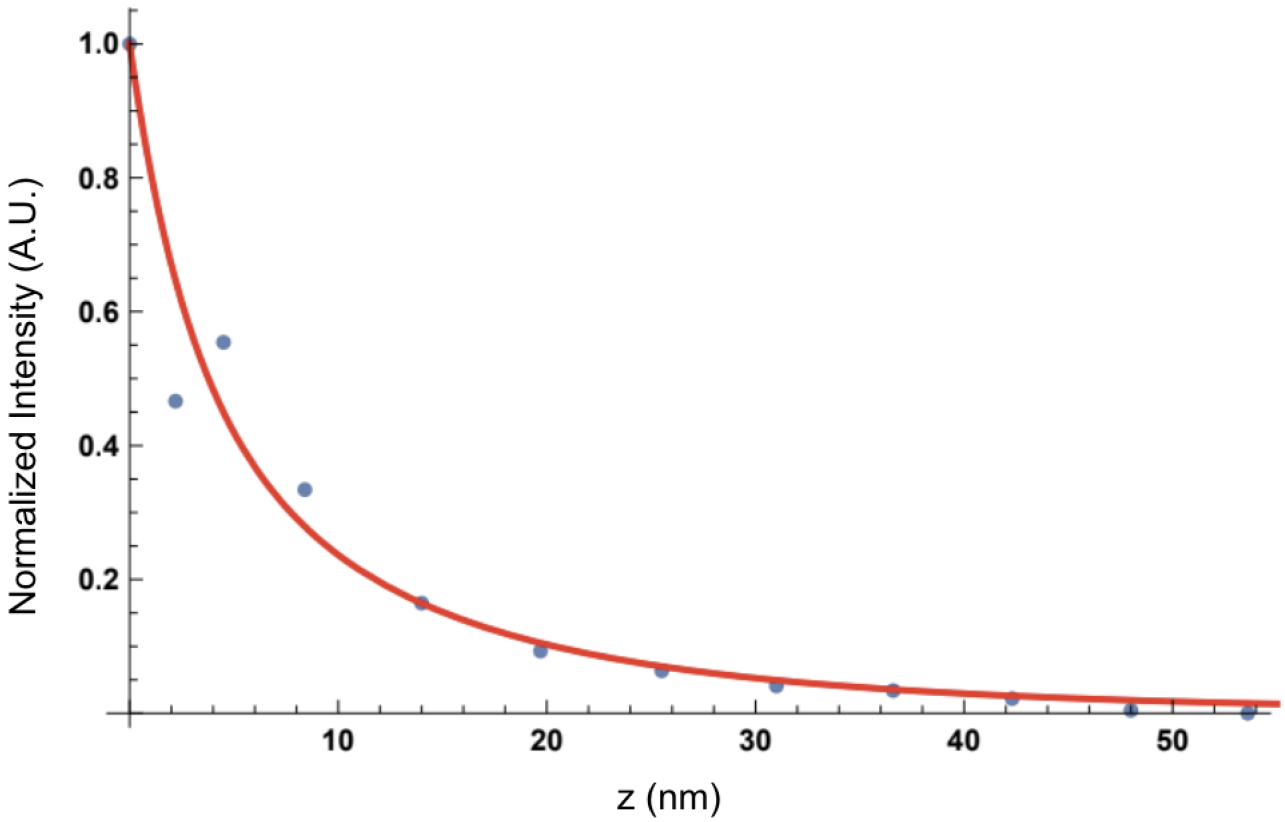

Figure A.1: Tip-approach curve fit
Fit of the graphene G' band data published in Ref. [28] and fitted using the proposed methodology.